2018

Surface Modification for the Improvement of Metal/Organic Semiconductor Interfaces

Jonathan Paul Hopwood

LOYOLA UNIVERSITY CHICAGO

SURFACE MODIFICATION FOR THE IMPROVEMENT OF METAL/ORGANIC SEMICONDUCTOR INTERFACES

A DISSERTATION SUBMITTED TO

THE FACULTY OF THE GRADUATE SCHOOL

IN CANDIDACY FOR THE DEGREE OF

DOCTOR OF PHILOSOPHY

PROGRAM IN CHEMISTRY

BY

JONATHAN P. HOPWOOD

CHICAGO, IL

AUGUST 2018

ACKNOWLEDGEMENTS

Over the last 5 years, there have been many people who have helped and supported me who deserve my sincere thanks. First, I would like to thank my advisor Dr. Jacob W. Ciszek who graciously allowed me to join his lab. Throughout my time at Loyola University Chicago, Dr. Ciszek has been instrumental to my successes, both at the bench and as a writer, and has continued to give his support and opinions for topics in chemistry as well as those found outside our field. I am grateful for your patience when experiments went awry or when I didn't understand or forgot various concepts. I appreciate the time you spent training and mentoring me. Second, I would like to thank my committee members Dr. Jan Florian, Dr. Dan Killilea, and Dr. Paul Vadola for serving on my committee as well as their input and advice on my projects. I would also like to thank the Arthur J. Schmitt Foundation who provided the funding for my last year of my graduate studies.

I would also like to thank current and former graduate students Rachael Farber, Brittni Qualizza, Alexander Villani-Gale, Kyle Webster, and Daniel Catlin along with undergraduates Shawn Dalke, David Turner, Haejun Park, Selma Piranej, and Demetra Adrahtas for their continued support, the many discussions we had, and offering their help when I needed it. A special thanks goes to Gregory Deye who worked alongside me for the last three and a half years; through all the ups and downs you have been a great friend and a pleasure to work with.

I also want to thank my family and friends who provided the emotional support I needed along the way as well as the often much needed mental breaks from chemistry. Finally, my

fiancé Sandy Nahra, who I will never be able to thank enough for the day-to-day support you have given to me over the last four years. You have been there to listen when I needed to vent, offered advice when I needed it, and made me laugh when I needed cheering up. I am excited to begin this next chapter of life with you.

TABLE OF CONTENTS

LIST OF TABLES

LIST OF FIGURES

LIST OF SCHEMES

CHAPTER ONE

AN INTRODUCTION TO CHEMISTRY AT THE METAL/ORGANIC INTERFACE

As the 21st century comes into its own, humanity has become surrounded by electronic devices and is even defined by one's interactions with them. These devices range in size and use, from the small fitness tracker to the 72-inch 4K television, but nonetheless play an integral part in modern life. As technology expands, so does our imagination and devices become integrated into everyday items. Illustrative of this cyclical relationship, the development of cheap and lightweight electronics gave rise to displays that could fit in a pocket or hang on a wall. Today, the cycle continues with the application organic semiconductors into electronics, leading to the creation of flexible devices. Imagination, in turn, has taken the prospect of flexible devices in full stride and has led to the development of wearable technology, including products such as the TempTraq®, a digital thermometer applied onto the skin, as well as glucose sensing contact lenses.[1] As technology and imagination continue to fuel each other, new applications are endless.

These smart devices can be broken down into discrete electronic elements, each performing a critical function. One of the most important is the field-effect transistor (FET), which is an electrically controlled switch that allows the device to perform a particular function. Typical construction of a FET consists of source and drain electrodes in contact with a semiconductor that is insulated from a third electrode, known as a gate, all supported by a substrate (Figure 1a). Conductivity of a FET is controlled by an electric field that is turned on or off when a potential is applied to the gate electrode. Typically, the source and drain electrodes

are made of a metal, often copper, while a doped silicon (or germanium) semiconductor is used for the channel between the contacts. For FETs, there are two possible configurations for the source and drain electrodes: bottom- and top-contact. For bottom-contact FETs, the electrodes are deposited onto the dielectric with the semiconductor deposited on top. On the other hand, top-contact FETs have metal electrodes located on top of the semiconductor (Figure 1a). This layering and configuration will become important in the projects herein.

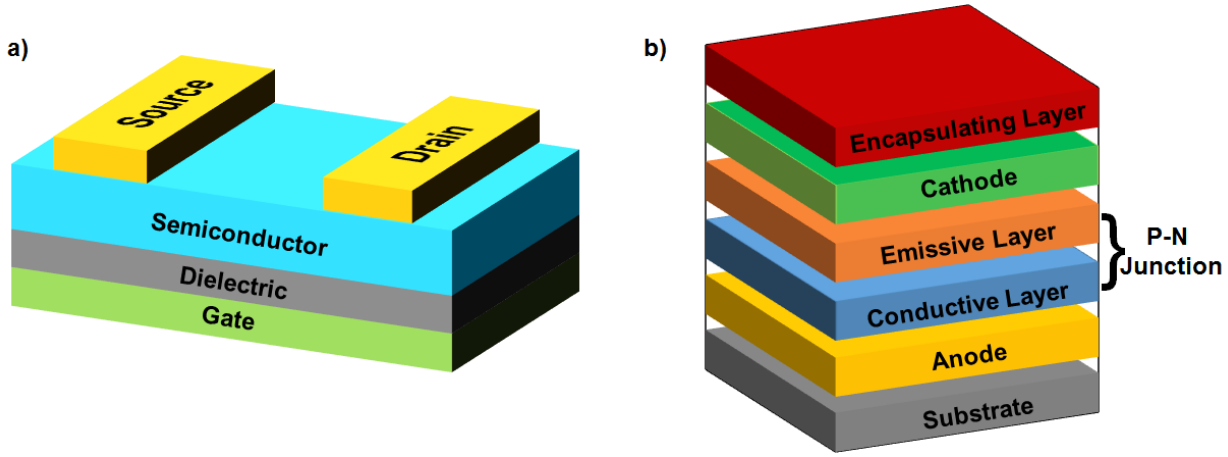

Figure 1. Typical constructions of (a) a top-contact FET and (b) LED.

The second component is the light emitting diode (LED, Figure 1b). Along with the metal contacts and substrate, there are two semiconducting layers. The first is a p-type semiconductor, which the primary charge carriers are holes, that is connected to an n-type semiconductor, which conducts electrons. Typical semiconductors include GaAsP and GaP. The working principle of an LED is that when an electric field is applied to the device, the hole and electron combine at the interface between the two semiconductors (p-n junction). This allows for the release of energy as a photon of light. Through tuning the band gap at the p-n junction, the wavelength of the emitted photon can be controlled. As implied by the materials that make up its construction, FETs and LEDs are rigid devices with limitations for functionality and applications.

Due to the demands brought by smart devices (e.g. flexibility, low cost, customizable), organic semiconductors have been sought as replacements for inorganic semiconductors. As a result of their molecular nature and tunable properties, organic materials can address many of the requirements of the next generation of devices. Over the last two decades, many studies have demonstrated competitive charge carrier mobility,[2,3] solution processable semiconductors, and the development of techniques to either deposit or print the organic materials onto various substrates.[4–8] Device architectures have evolved notably via improved electrodes and insulating layers, as well as encapsulating layers that prevent oxidation while still allowing for flexibility. These new characteristics have been developed to the extent where devices are competitive with their inorganic analogues. Examples include the application of organic LEDs into mobile phones, to the point where most manufacturers have adopted this technology. While substantial improvement has been achieved with the electronic components of a device, metal contacts are still required for functional devices. As a result, there is still a massive amount of improvement or added functionality that can be addressed at the metal/organic interface.

Metal Modification via Self-Assembled Monolayers

Illustrative of the improvements required of the interface is the energy difference between the metal and organic layers, known as the Schottky energy barrier.[9] Here, high contact resistance is generated from the misalignment of the metal's Fermi level with the highest occupied molecular orbital (HOMO) or the lowest unoccupied molecular orbital (LUMO) of the organic semiconductor. This misalignment is often the primary source of inefficiencies found within organic devices.[9,10]As a means to minimize the Schottky energy barrier, and increase device efficiency, Campbell and coworkers demonstrated that the addition of self-assembled

monolayers (SAMs) could shift the metal's Fermi level depending on the magnitude and orientation of the SAM dipole.[11,12] For example, when the SAM dipole vector is oriented away from the metal, the stabilization of the metallic electrons result in lowering of the Fermi level which in-turn increases the electron Schottky energy barrier with the organic LUMO. On the other hand, when the dipole vector is oriented towards the metal, the destabilization of the metallic electrons result in an increase in the Fermi level and a decrease in the electron Schottky energy barrier between the metal and organic LUMO (Figure 2). When incorporating this technique into devices, the hole energy barrier between silver electrodes and the organic semiconductor, triisopropylsilylethynyl pentacene (TIPS-pentacene), was decreased by using thiophenol, 4-fluorothiophenol, and pentafluorothiophenol SAMs.[13] Here, the monolayers successfully aligned the silver electrode Fermi level with the TIPS-pentacene HOMO and an increase in drain current was observed and that current was proportional to the magnitude of the SAM dipole. Another example was the decrease of the electron energy barrier between gold electrodes and a C_{60}, an n-type semiconductor, using SAMs consisting of methylbenzenethiol, aminobenzenethiol, and (dimethylamino)benzenethiol.[14] As a result of successful energy level alignment, a decrease in the threshold voltages for the SAM-modified electrodes were observed. The authors attributed this effect to the electron donating character of the SAMs.

With the addition of SAMs, further functionality can be added to organic devices to create "smart" devices. Examples of potential SAM-based smart electronics include flexible pressure arrays,[15] biosensors, and biocompatibile devices.[16,17] Switchable SAMs have also been studied, so that Schottky barriers can be controlled via an external stimulus, such as electrochemical potentials, via some change in the SAM dipole.[16] Similary, photochromic

molecules have also been integrated into interfacial SAMs and act as a photoresponsive switch.[18–21] In most cases, this switch is controlled by a photoisomerization that creates a dipole within the SAM and, in-turn, alters the work function of the metal via the mechanisms just discussed. These types of photoreversible work function alterations were first observed with the *trans-cis* photoisomerization of azobenzene monolayers.[22–24] Here, UV induced work function shifts were on the order of ~0.4 eV for unsubstituted azobenezene monolayers. With the addition of electron withdrawing cyano groups to the azobenzene, work function shifts were observed in the opposite direction. These types of photoswitchable SAMs were applied to OFETs and the device response was shown to be controllable via stimuli (i.e. light),[25] thus giving rise to a new form of smart electronic devices.

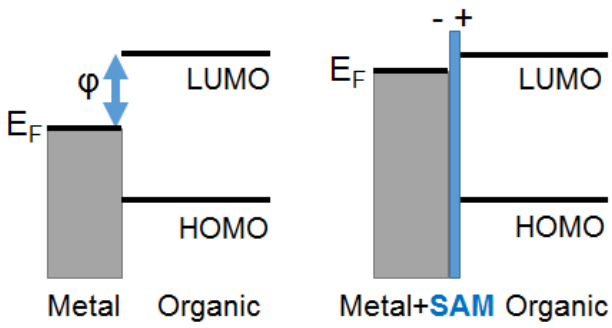

Figure 2. Decreasing the Schottky energy barrier (Φ) between a metal and organic semiconductor via the addition of a SAM containing a dipole vector pointed towards the metal.

In Chapter 2, this dynamic response was extended to another class of photochromophores, dihydroindolizines (DHIs).[26] The behavior of the DHIs were studied using polarization modulation infrared reflection absorption spectroscopy (PM-IRRAS) and UV-vis spectroscopy in order to ascertain how the phase of the DHIs and their proximity to a metal surface affected their switching capabilities. These surfaces are central to functioning devices, but are known to significantly diminish switching behavior.[27] Monitoring and quantifying the

extent of photoisomerization in DHI thin films allows for determination of the mechanism of inhibition, which was hypothesized to be steric effects, energy transfer, or electron transfer to the metal. DHIs are well suited for such a study because of their pronounced spectroscopic signatures (Figure 3). Here, monolayers and thin films of the DHI could be irradiated with UV light to induce the photoisomerization of the stable spiro form (Figure 3a), which can be readily observed via IR spectroscopy (Figure 3b). The extent of photoisomerization of DHI thin films indicate that switching is primarily affected by steric inhibition along with surface energy transfer. These finding were ultimately published in *Photochemical & Photobiological Sciences*.[28]

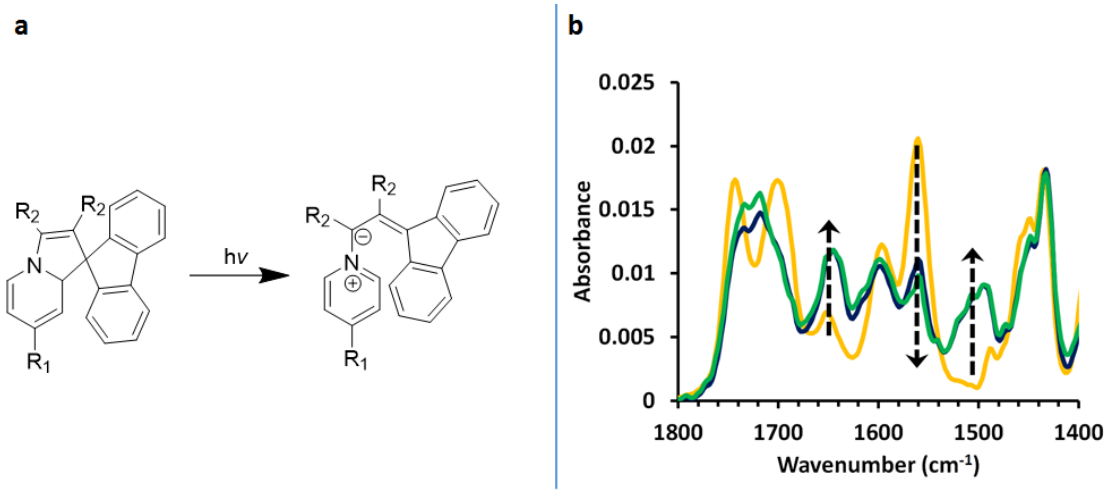

Figure 3. (a) Formation of the zwitterion via photoisomerization from the neutral (spiro) conformer. (b) Typical PM-IRRAS spectra of the DHI photoisomerization from before irradiation with UV light (yellow) to 2 (blue) and 8 (green) minutes.

Organic Semiconductor Modification

While the modification of metal surfaces has been shown to be an effective means of overcoming *some* interfacial challenges, organic semiconductor surfaces, conversely, have paltry means of control and need significant improvement. The materials themselves have been well developed resulting in many studies on various families of semiconductors, including small

molecules and polymers.[29–31] Examples of common semiconductors include both p-type and n-type semiconductors such as P3HT and fullerenes respectively (Figure 4). Of the small molecule semiconductors commonly investigated, the acene family is one of the more prominent classes. The acenes have been studied in much depth, especially pentacene due to its high charge carrier mobility, and have been utilized in TFT and OLED applications.[32–34] Although pentacene has many desirable characteristics, its tendency to undergo photooxidation, as well as its cost, means that tetracene is often used as an analogue. Together, these two molecules have produced a plethora of research, ranging from optimizing molecular orientation and film growth[35] to studying contact effects.[36,37] Further development in solution-processable films (e.g. TIPS-pentacene) has also been achieved.[38,39] Despite all the progress made with the acene family, a litany of interfacial issues still exist. Of particular concern is the weak interfacial interactions between the acene and the metal electrode. These weak interactions manifest themselves into problems such as delamination and metal penetration.[40] In order to overcome such limitations, a solution is needed.

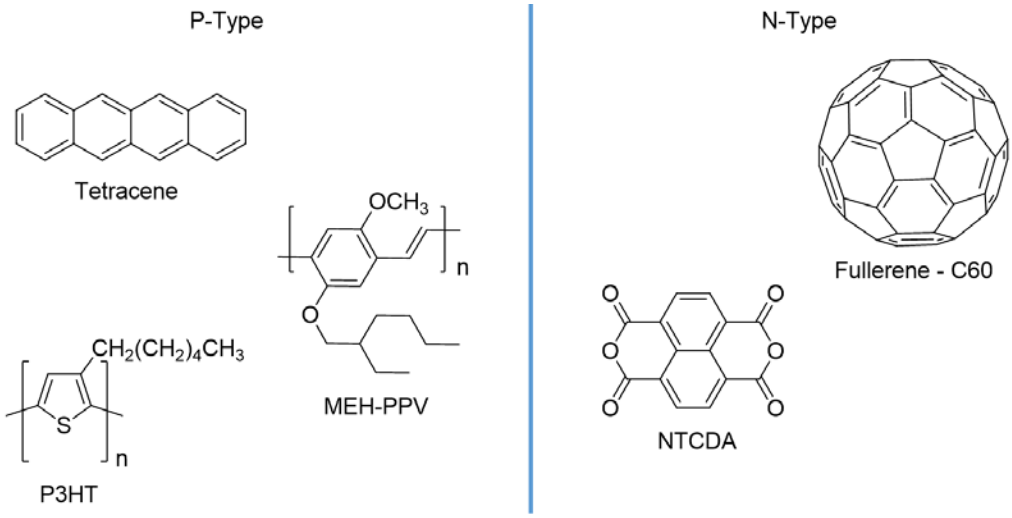

Figure 4. Common p-type and n-type organic semiconductors used in organic electronics.

Inspired by SAMs on metals, I proposed to study SAMs on organic semiconductors to address problems of poor adhesion and reducing metal penetration. Here, if the terminal functional group has a functionality that coordinates a deposited metal, metal adhesion would greatly improve.[41,42] A good example would be comparing a SAM of octanethiol to that of octanedithiol as studied by Ohgi and coworkers.[43] The former contains a methyl group as the terminal functionality, which poorly coordinates to gold, while the latter's thiol group does so with high affinity. Upon deposition of gold onto the SAMs, a uniform overlayer was observed via STM on only the octanedithiol SAM. Electronic measurements of this sample resulted in a small capacitance, indicating the presence of a true overlayer separated from the Au(111) via the SAM. If this is the case, SAMs should be a suitable means of improving metal adhesion of an organic semiconductor thin-film. This is important as often the metal must be deposited onto the organic semiconductor, meaning the chemistry must be applied via the organic semiconductor.

In Chapter 3, the extension of SAMs to tetracene films was applied for the improvement of interfacial adhesion. Functionalities that promote strong adhesion between a metal and the organic film can be easily installed via just two steps. The first is via the Diels-Alder reaction, which has been proven to be a well-suited means to append further reaction sites to the surface of acene thin films.[44] Such Diels-Alder reactions are readily performed with maleic anhydride. The second step consists of reactions of primary amines with the anhydride adducts. These reactions were performed in order to install more desirable functionalities, such as thiols and carboxylic acids, as dienophiles containing such functional groups were unsuitable for the solid-vapor chemistry that is utilized on the films. In order to characterize the reactions, the surface species were analyzed by infrared spectroscopy, X-ray photoelectron spectroscopy (XPS), and mass

spectrometry. Peel tests indicate the adhesion of metalized films to reacted films is improved, thus demonstrating secondary reactions as a means of improving interfacial flaws.

Concluding Thoughts

With the developed chemistry resulting in successful adhesion, further routes of exploration are limitless. One direction would be towards the application of biosensing. Installation of an amine on the surface, via a secondary reaction with ethylenediamine, would readily provide a desirable locus for the addition of a biomolecules. Another is that I hope that flexible substrates, such as PET, will be at some point be implemented so that the number of bend cycles of the films could be determined. If this chemistry shows to be useful for flexible substrates, this could open many doors for the development of this and similar chemistries.

Whether or not the Diels-Alder reactions on acene films will be used in an industrial setting, I believe that this work lays the groundwork for future surface functionalization of organic films. Furthermore, the development and application of surface analysis techniques, in particular MALDI-TOF, as a means of analyzing thin films will be a powerful tool for the advancement of this field. It is my hope, that organic semiconductors become standard in all devices, and in turn continue the cycle that inspires new and imaginative applications, materials, and chemistries.

CHAPTER TWO

SOLID STATE AND SURFACE EFFECTS IN THIN-FILM MOLECULAR SWITCHES

Introduction

In a drive towards smart materials, photoswitchable elements are regularly added to metallic interfaces. Here, these elements can act as regulators of organic field-effect transistors and organic light emitting diodes,[45–47] or impart motion to micron scale objects.[48,49] From an application standpoint, these surface based photochromophores are exciting proof of principles for the field. However, when the switches are interfaced with a surface, their already complex photoprocesses become exponentially more so.

In solution, a molecular switch responds to light by becoming excited and multiple processes can follow, including fluorescence and internal conversion. Along with these familiar processes, a molecular switch has the unique ability to isomerize to a structurally distinct state (Figure 5, right).[50] This "switched" state can be reached via ring-closing/ring-opening,[51] *cis-trans* isomerization,[52] and can even involve the formation of a zwitterion.[53] Generally, a color change accompanies switching, hence the moniker "photochromophore". Established classes of photochromophores have been optimized such that the molecule's structure and electronics impart switching kinetics that compete effectively with the relaxation processes listed above.

When interfaced with a metallic surface, the photochromophore's behavior is altered due to surface effects.[27,54] In particular, the switching efficiency of these systems can be significantly less than that of analogous solution based systems, with both the molecular environment and the

surface playing the major roles.[27,55,56] The former is general to switching in the solid state, and is a result of the steric environment around the photochromophore (Figure 5, top left).[57,58] The latter is specific to the metal surface, and here excited adsorbates now also relax via non-radiative decay to the surface, the two primary modes being electron and energy transfer (Figure 5, left).[59] Theory also predicts that electron transfer is to supplant energy transfer as the primary mode of non-radiative decay within 1-2 nm to the surface.[59]

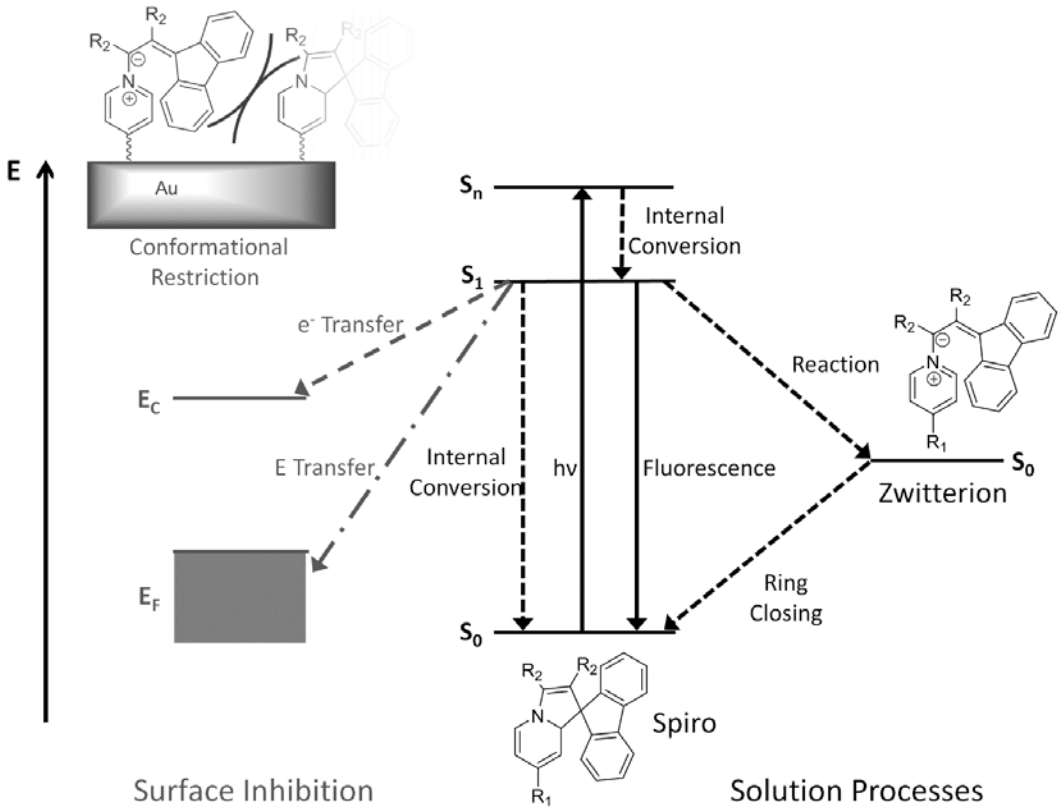

Figure 5. Jablonski diagram depicting photoswitching and quenching mechanisms for the dihydroindolizine (DHI) system. Top left depicts steric inhibition whereby a neighboring molecule prevents switching in the solid state. The lower left displays quenching via electron transfer to the metal's conduction band ($E_{c)}$ and energy transfer to a metal surface. In the middle and to the right, typical decay mechanisms for photochromophores are shown, including the production of the switched state (zwitterion).

With so many competing processes, it is natural to examine them serially such that the complex processes at surfaces can be teased apart. Herein we describe the design and transfer of three dihydroindolizine (DHI) photochromophores from solution phase to solid and thin-film, while examining the relative inhibiting factors that appear with each change. Specifically, through the use of UV-vis and IR spectroscopy, we characterize optical properties and spectroscopic markers for each DHI as well as quantitatively measure the extent of switching with thin-film IR studies.

Experimental

All chemicals were purchased from Sigma Aldrich or BDH and used without additional purification. **DHI-1**, **6**, and **14** were synthesized using previously reported methods,[26,60,61] and the synthesis for **DHI-9** is located in Appendix A. DHIs were kept in the dark at all times except during irradiation.

Metal evaporations were performed using a Kurt J. Lesker NANO 38 thermal evaporator. Solution UV-vis characterization of the DHIs was performed using a Shimadzu UV-2550 spectrophotometer in CH_2Cl_2. Bulk DHI films on NaCl salt plates were studied via a Bruker Optics Tensor 37 FT-IR with a MCT detector and a Shimadzu UV-2550 spectrophotometer. DHI thin-films were prepared using a Headway Research Inc. 1-EC101D-R485 photo-resist spinner. The thin-films were studied via surface IR using a Bruker Optics Tensor 37 FT-IR with a polarization modulation accessory (PMA 50) and MCT detector. Thin-film thicknesses were measured using a Gaertner Stokes ellipsometer.

Bulk Films on Salt Plates

DHIs were dissolved in dichloromethane with concentrations ranging from 1 to 2 mg/mL. 1 mg of the DHI solution was placed on the NaCl salt plate and the solvent was allowed to evaporate. A UV-vis spectrum, followed by an IR spectrum, was taken for the spiro form. The sample was then irradiated for 2, 8, and 13 min with spectra taken after each time interval. Indexing was used to maintain analysis of a consistent region.

Thin Film Preparation

Substrates were prepared as follows: glass slides were cleaned with piranha solution (3:1 H_2SO_4:H_2O_2) for 30 min at ~100 °C and rinsed copiously with 18 MΩ·cm water. Slides were then dried with nitrogen and placed in the thermal evaporator. Silver (50 nm), followed by gold (50 nm), was evaporated onto the slides with a chromium adhesion layer (5 nm) at a base pressure $<1\times10^{-6}$ Torr and a deposition rate of 1 Å/s. Directly after evaporation, gold substrates were placed onto the spin coater and the DHI solution was cast onto the substrate. Solutions for spin coating consisted of the DHI dissolved in dichloromethane, at concentrations ranging from 0.5 to 2 mg/mL. Initial spin speed was held at 100 RPM for 5 seconds and was then increased to 1000 RPM which was then held for 15 seconds for all samples. High concentrations were used for the thicker samples; dilute was used for the 5 nm samples. The thickness for the thin-films denoted as “30 nm” herein ranged from 28-32 nm, as determined by ellipsometry. For “~14 nm” thin-films, ellipsometric thicknesses were 8-14 nm. The 5 nm thin-films ranged ±0.5 nm.

Passivated Samples

Sample preparation used identical substrates to those prepared for the thin-films studies. After evaporation, a hexadecanethiol passivation layer was assembled. The passivation layer was

prepared by placing the gold substrate in a 0.4 mM hexadecanethiol in a N_2 purged 200 proof ethanol solution for 5 h. The sample was then rinsed with ethanol (×3), sonicated in ethanol for 30 s, rinsed with ethanol (×3), and finally dried with nitrogen. Upon successful self-assembly, **DHI-1** was dip-coated onto the slide from a 2 mg/mL solution in a 2.5:1 hexanes: dichloromethane mixture. Ellipsometric thicknesses for both the passivation layer and thin-film are reported in the text.

Photoswitching Studies

DHIs films were irradiated with a 400 nm LED source (12 mW/cm^2). The LED rastered ~1 cm over the film for 2, 8, and 13 min.

Results and Discussion

Molecular Design, Synthesis, and Solution Behavior

In the design of the molecules, two main things were considered. First, the molecules discussed herein were designed to isolate factors affecting the switching of adsorbed DHI monolayers on a metal surface by incorporating systematic variation of the linkers that tether them to that surface (i.e. Figure 6, left). Specifically, the bolded grey linkers in Figure 6 were chosen to have similar lengths (and thus surface-photochromophore distance), but at the same time contain dramatically different electronic transfer ability. Full details on the implications of the various linkers in the context of monolayer studies are described at the end of this chapter. The second factor we considered was the electron donating/withdrawing capabilities of the group attached to the dihydropyridine ring.[62] By intentionally choosing linkers with similar donating abilities, the three DHIs listed in Figure 6 should have the same stability in the zwitterion (switched) form, as well as optical properties (DHIs being exponentially more sensitive to

changing the methyl ester and fluorene substituents).[50] The only complication with our molecules is that the first design parameter requires full conjugation for at least one of the linkers, a change that can have a non-negligible impact on switching. To minimize this effect, linkers are located at the 7′ position, where effects of conjugation are extremely small, primarily due to cross-conjugation.[62]

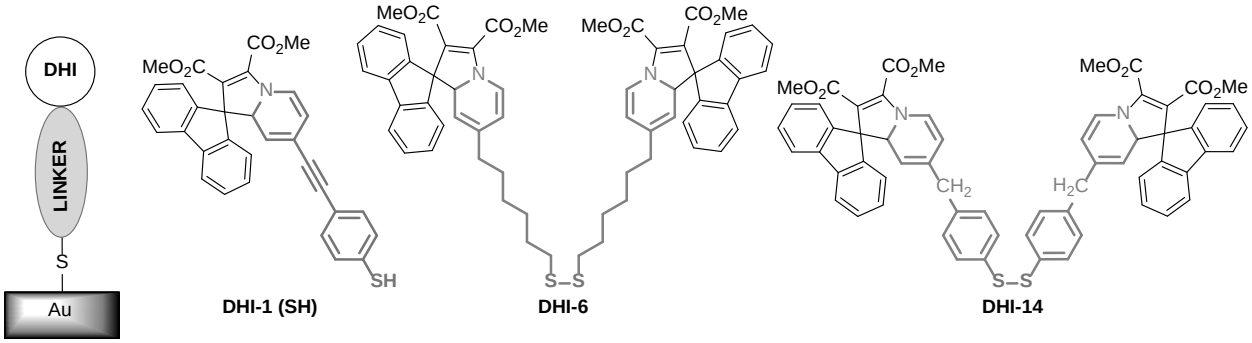

Figure 6. Structures of **DHI-1**, **6**, **14**. Linkers for surface attachment are indicated in bolded grey and utilize gold-thiol chemistry for self-assembly.

The switches were synthesized via reported protocols,[26,60,61] and their optical properties were confirmed via UV-vis. Here, characteristic bands related to the switch state of the molecules can be readily observed (the π- π* transition for the spiro form and the presumed charge transfer transition for the zwitterion). In Figure 7, the π- π* transitions of the spiro DHIs are shown, with an example of the presumed charge transfer transition of the zwitterion in the inset. The λ_{max} for the spiro and betaine forms, along with extinction coefficients (ε), are summarized in Table 1. As expected, the majority of optical properties are notably quite similar, with the exception of a slight shift in **DHI-1's** π- π* absorption which is red-shifted on the account of the extended conjugation system within the oligo(*p*-phenylene-ethynylene) linker.[62] Half-lives of the zwitterion ($\tau_{1/2}$), which were determined by monitoring the decrease of the presumed charge transfer transition over time and modeling the transition as a first-order

decay, were also relatively similar.[50] The longer half-life observed for **DHI-1** can be attributed to the delocalization of the zwitterions charge within the conjugated oligo(*p*-phenylene-ethynylene) linker in **DHI-1**.[62] Complete UV-vis characterization and relaxation experiments can be found in the Appendix A, Figure S1.

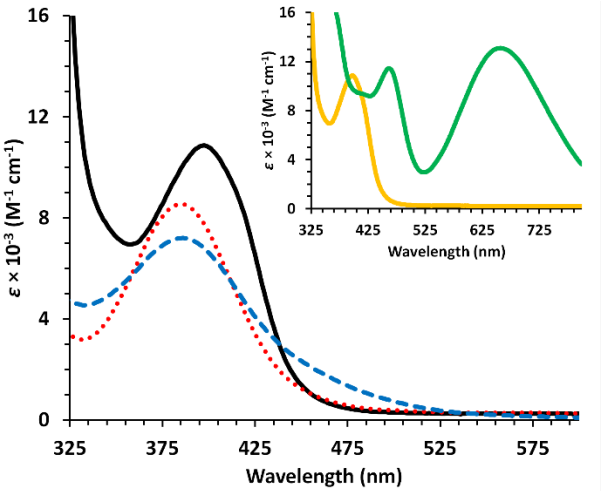

Figure 7. UV-vis spectra of DHI-1 (black solid line), 6 (red dotted), 14 (blue dashed) in dichloromethane. Inset: Upon irradiation of the spiro conformer (yellow) of **DHI-1**, a peak at 657 nm was observed indicating the formation of the zwitterion (green).

Table 1. Optical properties of **DHI-1**, **6**, and **14**.

DHI	λ_{max} (nm)	$\varepsilon \times 10^{-3}$ (M^{-1} cm^{-1})	Zwitterion λ_{max} (nm)	$\tau_{1/2}$ (s)
1	397	11	657	115
6	385	8.5	586	66
14	386	7.2	602	47

Bulk Photochemical Properties and Spectroscopic Markers

When moving to the solid state studies, experiments are limited by the fact that UV-vis does not provide the sensitivity necessary to study thin or monolayer films. To circumvent this, characteristic DHI IR vibrations are correlated with a change in optical absorption and molecular structure. Various IR techniques, such as polarization modulation infrared reflection absorption

spectroscopy (PM-IRRAS), do have the sensitivity to measure these vibrations in thin-films (vide infra). For IR/UV-vis correlation experiments, the DHIs are examined as a micron thick film on a salt plate, which is photoconverted via irradiation, while observing both UV-vis and IR signatures. Relaxation for these DHIs is extremely long in the solid state relative to the solution phase materials,[26] and thus has negligible effect on these (and later) measurements.

Before irradiating the samples, it was observed that the π-π* transition had red-shifted slightly for **DHI-6** and **DHI-14** (395 and 396 nm respectively, Figure 7). It is possible that this effect could be attributed to the lack of solvation and thus a higher ordering of the DHIs. However, this trend does not appear to be systematic as the same red-shift was not observed for **DHI-1**. Despite this inconsistency, it is beneficial for our studies due to the consolidation of λ_{max} near 400 nm which allows for the use of a single monochromatic irradiation source for all samples.

Upon irradiation with 400 nm light, a stretch correlated to the coupled double bond vibrations within the dihydroindolizine decreased (1559 cm^{-1}) while the stretch correlating to the pyridinium ion appears (1506 cm^{-1}), indicating the formation of the zwitterion in **DHI-6**.[26] We show in Figure 8, that this is in fact characteristic of the DHIs, and can be correlated with the extent of switching observed in UV-vis. As shown in Figure 8, a decrease in absorbance for the π- π* transition peak (~400 nm), as well as an increase in absorbance for the presumed charge transfer transition (500 – 700 nm), occurs in tandem with the decrease in absorbance at 1550-1559 cm^{-1} for **DHIs 1**, **6**, and **14**. At the same time, an absorbance appears between at 1500-1506 cm^{-1} for **1**, **6**, and **14**, along with a secondary feature at 1637, 1643, and 1641 cm^{-1} for **1**, **6**, and **14** respectively. Together, these stretches indicate the formation of the zwitterion. As the

thickness is decreased from the micron scale bulk films to nanometer scale thin-films, the aforementioned stretches, in particular the stretch at 1550-1559 cm^{-1}, will be used as a spectroscopic marker. The rationale behind this marker is twofold. First, the other IR modes which have pronounced changes in Figure 8 (increasing at ~1640 cm^{-1} and 1500 cm^{-1}) cannot be effectively used due to overlapping stretches in the neutral molecule in the former and surface selection rules associated with the latter.[26,63] Second, the stretch at ~1560 cm^{-1} occurs *only* in the neutral form[26] and hence it can be used as a semi-quantitative measure of switching.

There is one other noteworthy attribute of the solid state switching. When moving to the solid state, the relaxing of the zwitterionic species decreases dramatically, resulting in much longer half-lives. For example, the half-life of **DHI-14** increases from 47 s in solution to 3.2 h in the solid state. The implications for experiments are, again, positive. As relaxation is on the hour scale, it is no longer a competing process and has minimal effect on measurements of switching kinetics. This also mitigates half-life differences present in solution; back (relaxation) reaction is effectively a non-contributor amongst the competing processes shown in Figure 5.

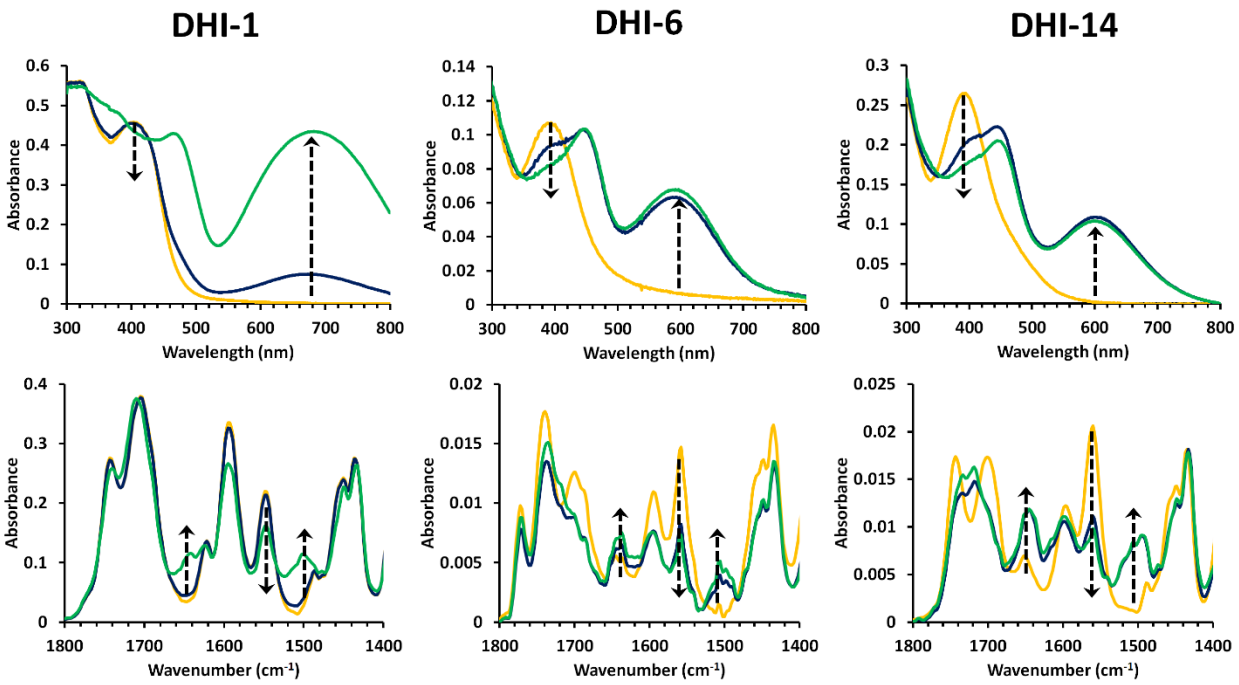

Figure 8. UV-vis and FTIR (NaCl plate) spectra for bulk **DHI-1**, **6**, and **14**. The spiro conformer (yellow) was irradiated for 2 (blue) and 8 (green) min.

Thin-Films and Steric Inhibition of Switching

Bulk samples were useful in correlative studies, but lack the precision necessary for analyzing relative switching states in the solid state. Thus, all three DHIs were examined as 30 nm thick films on gold substrates. Thin-film ellipsometry confirmed that all samples are uniformly coated, and thicknesses deviated by ~3 nm over a typical sample. When analyzed by PM-IRRAS, the diagnostic signals for the spiro form were apparent. It is interesting to note the difference between the films on the NaCl and gold substrates, in particular the carbonyl stretch near 1700 cm^{-1}, which is lower in intensity compared to the rest of the spectra (Figure 8, 9). This has been observed before in previous works, and is confined to the spin-coated samples (not self-assembled monolayers or dropcast films).[26] These effects arise from the partial alignment of

spin-coated molecules in the plane of the film[64] with the carbonyls now oriented along the same axis, and the molecular dipole offset by a surface image dipole.[63]

These samples were irradiated with a 400 nm LED at an intensity of 12 mW/cm^2. As described earlier, the vibration at 1550-1560 cm^{-1} corresponds only to the spiro form, and hence its consumption can be used semiquantitatively to indicate the extent of switching.[26,63] For example, the 57% decrease of intensity at 1559 cm^{-1} for **DHI-6** indicates roughly 57% of molecules present have been photoconverted (Figure 9). Accordingly, the switching kinetics were as follows. For the 30 nm thin-films of **DHI-1**, after 2, 8, and 13 minutes of irradiation, the stretch at 1550 cm^{-1} has decreased by 20%, 32% and 38% respectively. Thin-films (30 nm) of **DHI-6** were observed to switch 57%, 68%, and 74% after 2, 8, and 13 min of irradiation respectively while for **DHI-14**, switched 27%, 40%, and 44% after 2, 8, and 13 min of irradiation respectively. The data (also shown in Figure 9) highlight the fact that when moving from solution to solid state, appreciable differences arise between the molecules. It is clear in Figure 10 that **DHI-6** significantly outperforms **DHI-1** and **DHI-14** (despite having a smaller ε than **DHI-1**). Notably, a higher percentage of **DHI-6** molecules had formed the zwitterion *after 2 min of irradiation than for the other DHIs after 13 min.*

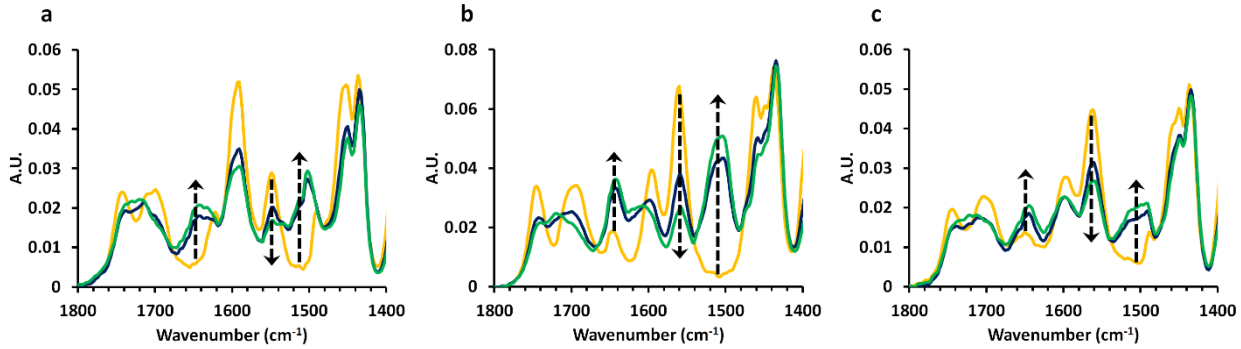

Figure 9. PM-IRRAS spectra of **DHI-1 (a)**, **6 (b)**, and **14 (c)** thin films (30 nm) on gold substrates. The spiro films (yellow) were irradiated for 2 (blue) and 8 (green) min.

A potential explanation for this diminished switching would be the steric environment surrounding the photochromophore. Under such circumstances, it would be expected that flexibility of the linker (alkyl chain versus rigid oligo(*p*-phenylene-ethynylene)) would heavily impact the extent of switching, similar to that found in photoswitchable polymers.[65] This was tested using **DHI-9**; a simple photoswitch containing only a methyl group as the "linker".[62] Due to the small size of the linker, photoswitching should display minimal steric effects, but is electronically similar to both **DHI-6** and **DHI-14**. Therefore, if similar switching is observed to that of **DHI-6** (assuming some dilution factors from the alkyl chain) the flexibility of the linker can be confirmed as a probable cause of the observed difference in switching. This was observed to be the case (Figure 10). As shown in the figure, there is a distinct difference between the mean switched percentage for DHIs **1** and **14** (36% and 44% respectively, at 13 min) when compared to **6** and **9** (74% and 64% respectively), suggesting that the flexibility of the linker does affect the switching capability of the DHIs.

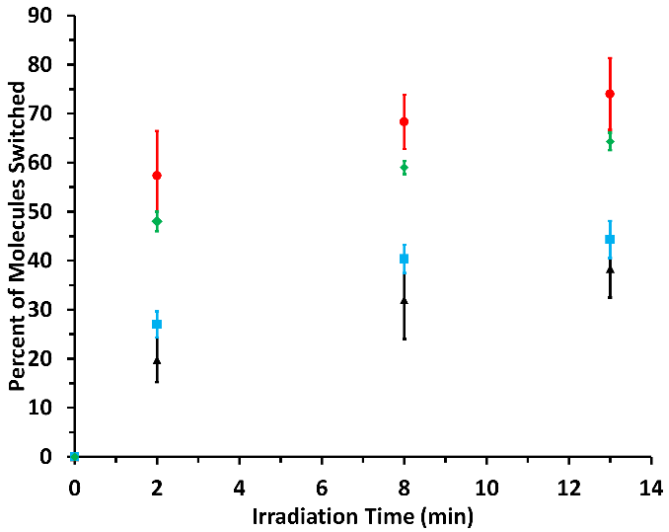

Figure 10. Percent of **DHI-1** (black triangles), **DHI-6** (red circles), and **DHI-14** (blue squares) molecules in the zwitterion form as a function of irradiation time for the 30 nm. Percent switching of 30 nm **DHI-9** (green diamonds) films were also measured in order to examine steric effects.

Moving to Monolayers: Electron and Energy Transfer Considerations

Of central interest to this work is the relative contribution of energy and electron transfer to the diminished switching observed in thinner films. In terms of energy transfer, theory described by Chance, Prock, and Silbey (CPS) states that the most significant component is a strong distance dependence ($1/d^4$).[59,66,67] Accordingly, linker lengths for the DHIs were similar (Table 2). Contributions of linker structure to energy transfer (i.e. via index of refraction) are minimal.[68,69] However, the different linker structure manifests itself in dramatically different electron transfer rates. For **DHI-1,** the conjugated oligo(*p*-phenylene-ethynylene) linker presents a relatively low tunnel barrier for electrons, while **DHI-14** contains a methylene spacer between two aromatic rings, and **DHI-6** a saturated alkyl chain, each with progressively slower electron transfer rates. This results in an effective range of electron transfer rate of 25 (Table 2). When comparing across DHIs, if switching rates are observed to vary by a substantial amount, then the results would suggest electron transfer as the dominant mechanism. If the three DHIs exhibit similar switching rates, the result would indicate energy transfer as the dominant mechanism.

Table 2. Physical and electrical properties of **DHI** linkers **1, 6,** and **14**. Relative energy transfer rate constants ($k_{rel,\ ET}$) were calculated using CPS theory,[66] while electron transfer rate constants ($k_{rel,\ e-}$) were calculated using linker length and electron decay constants (β).[54] Electronic decay constants were estimated from references 10 and 70.

DHI	Linker Length (Å)	$k_{rel,\ ET}$	$k_{rel,\ e-}$	β ($Å^{-1}$)
1	11.4	1.1	25	0.94
6	11.7	1	1	1.2
14	9.7	1.7	13	1

We begin to look in this direction by examining thinner films. In changing the thickness, the relative contribution of surface effects (namely inhibition based on energy/electron transfer) plays a proportionally larger role. DHIs were examined at 30 nm, ~14 nm, and 5 nm thickness, and complete IR/photoswitching data sets can be found in Figure S2 (Appendix A). These data sets can be summarized by comparing the percent of molecules switched at 30 nm to that at 5 nm, for each of the DHIs. The fraction of uninhibited switches was calculated for each DHI by dividing the percent switched at 5 nm by the 30 nm data. As shown in Figure 11, the DHIs are impacted by the metal as the sample begins to approach monolayer thickness. Here, the fraction of uninhibited switches for both **DHI-6** and **DHI-14** was calculated to be 0.65 and 0.70 respectively (at t = 2 min), indicating that the 5 nm films do not switch as effectively as the 30 nm film. A similar fraction is observed for **DHI-1** (0.86), though the inhibition less pronounced. It should be noted, however, that **DHI-1** is consistently the least effective switch out of the three DHIs examined, and accordingly, the amount of uncertainty between similar spectra is higher. Results at 8 and 13 min (which show more similarity with **DHI-6** and **DHI-14)** suggest that differences between the DHIs are minimal, and that in all three cases, thinner films were less effective switches. Seeking additional evidence that the surface was indeed the source of dampened switching, the spacing between the metal and photochromophore was lengthened, while the film was kept constant at 5 nm. A hexadecane thiol passivation layer provided a 2.1 nm gap between the DHIs and the metal, almost eliminating energy ($\sim 1/d^4$) and electron ($\sim e^{-d}$) transfer.[71,72] Ultimately, the passivated **DHI-1** films (4.9 nm) showed an increase in switching, compared to non-passivated **DHI-1** on gold (4.9 nm), and their kinetics are indistinguishable from the 30 nm samples. The results indicate that inhibition is from the metal/chromophore

coupling, rather than interfacial phenomenon (sterics at the surface, increasing surface/bulk ratio, etc.).

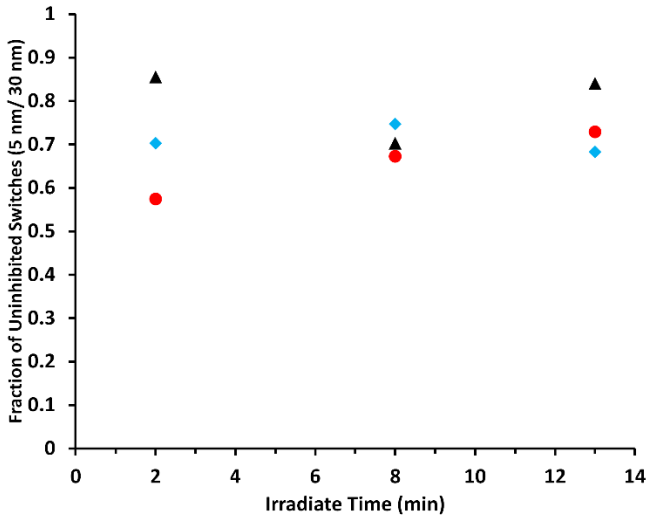

Figure 11. Fraction of **DHI-1** (black triangles), **DHI-6** (red circles), and **DHI-14** (blue squares) switches that are uninhibited in 5 nm films as a function of irradiation time.

These results are suggestive as to the mechanism of switching inhibition at this length scale. First, for the 5 nm films (4 molecules thick) the fraction of uninhibited switches is roughly 0.70 (Figure 11) when compared to the 30 nm films (roughly 24 molecules thick). As the switching effectiveness (and kinetics) of thinner films, even at 5 nm, still largely mirror that of the bulk samples, this lends credence to the assumption that inhibition is confined to the closest layer or two to the metal surface. This is not terribly surprising as electron transfer is not efficient until the surface-photochromophore distance is on the order of 1-2 nm, and energy transfer is focused on a region less than 10 nm from the metal surface.[68,73] Second, the fact that all samples display similar drop offs in switching (~0.30 inhibited) suggest energy transfer likely plays the dominant role. The role of electron transfer was not statistically significant at the length scales we examined, but cannot be discounted.

Finally, the data is also exceptionally clear on the challenging interplay between electronic structure and solid state switching behavior. From the 5 nm thin-film data (Figure S2, Appendix A), **DHI-6** still displays dramatically faster switching kinetics than **DHI-1** and **14**, even at these small scales. We predict that this trend will likely continue to the monolayer regime. This behavior serves as a possible explanation for the lack of switching to date in **DHI-1** monolayers, while successful switching of **DHI-6** monolayers has been reported.[26] This also further highlights the fact that while electron/energy transfer can be engineered into molecules, the changes to the structure required to do so often impact other factors affecting solid state switching (i.e. sterics). These findings, along with the extensive efforts that have been focused on DHI design,[60,62] will help shape future surface studies of this class of photochromophores in order to overcome the aforementioned challenges.

Conclusion

In summary, we have examined the extent of switching of molecular thin-films as a function of irradiation time to assess the impact of solid state structure and metal surface interaction on three similar photochromophores that display similar switching properties in solution. Solid state studies of thin-films on gold indicate that DHIs bearing rigid substituents are significantly inhibited, likely based on steric environment and conformational degrees of freedom. As all DHI films become thinner, metal surface based phenomenon become an increasingly important component and the average fraction of inhibited switches is calculated to be 0.30. The comparable drop-off in switching, despite structural motifs both inducing and repressing electron transfer, suggest that these systems are primarily inhibited via photochromophore/surface energy transfer. Lastly, the data obtained highlight the interplay

between molecular design, electronic structure, and switching efficiency, a challenge that will continue to impact future photochromophore designs.

CHAPTER THREE

SECONDARY REACTIONS OF FUNCTIONALIZED ACENE THIN FILMS

Introduction

The application of self-assembled monolayers (SAMs) in organic devices has revolutionized the electronics field.[74–77] Here, the interfacial interactions between metal contacts and the organic semiconductor are vastly improved through the application of a thin molecular layer which serves to improve contact resistance or mechanical properties critical to device performance. Significant progress has been made with respect to device performance through the use of SAMs by decreasing the Schottky barrier between the metal and organic semiconductor via energy alignment.[9,11,78,79] SAMs on the metal contact have also improved devices by optimizing orientation of an organic semiconductor in thin-film transistors (TFTs),[80] as well as through their use as a tether in self-assembled monolayer field effect transistors (SAMFETs).[81] The SAM chemistries involved in such devices are quite vast and range from thiols on gold, to phosphonic acids on silver,[82] to silanes on silicon oxide.[81] However, these advances come with a caveat. SAMs have been shown to be an effective solution for primarily bottom-contact configurations, while other device architectures have been neglected, despite the fact that many of the same problems plague these configurations.

The problems inherent to other architectures are readily illustrated by a top-contact device. Poor interactions between the deposited metal and underlying semiconductor can lead to poor adhesion between the two materials, which can cause overlayer delamination; weak

interactions similarly lead to metal penetration, which results in device failure via shorting. These challenges are present in organic light emitting diodes (OLEDs), where the metal overlayer/organic interfaces constitutes the final interface,[83] and often buffer layers must be used.[84] The solution should be simple. In fact, many of these very flaws have been examined previously using SAMs. To wit, it is well known that a SAM containing a thiol or carboxylic acid terminal group can improve both adhesion *and* metal peneration.[43,85] The challenge is our inability to install functional groups of this type as previously reported SAMs (Figure 12, center) are chemically ill-suited for fixing top contacts flaws in devices. Only molecules with smaller molecular weights, higher vapor pressures, and faster reaction rates have been successfully reacted, limiting the choice of terminal functional groups.[86–89]

As the chemical repertoire which can be directly generated on an organic semiconductor surface is limited, a workaround is needed. If the SAM functional groups are treated as a launching point rather than a final state, it is possible that these could be subsequently altered to a more useful terminus (Figure 12, right). Indeed, some functional groups, installed via a Diels-Alder SAM reaction,[87,88] provide a scaffold for further derivatization, specifically the maleic anhydride adduct. Secondary reactions with the maleic anhydride moiety can allow for the installation of a range of groups, including thiols and carboxylic acids, which are ideal for coordinating to deposited metals.[90] In this manner, functionalities incompatible with the Diels-Alder or molecules with low volatility can be introduced. This approach fixes metallization problems and also opens up the number of groups which can be installed for additional applications such as chemical sensing,[91] biofunctionalization,[92] and multifunctional polymer coatings.[93]

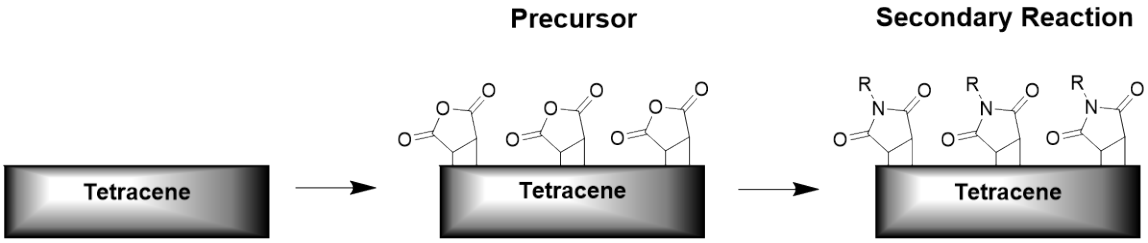

Figure 12. Functionalization of a tetracene film via previously established Diels-Alder chemistry to form the precursor anhydride films. Secondary reactions are performed to give the subsequent imide.

In order to produce a diverse array of surface functional groups, we perform derivatization reactions on already existing SAMs on acenes in order to tailor the terminal functional group. Using the maleic anhydride functionalized tetracene thin films as a precursor for further functionalization, we detail the successful secondary reactions of using primary amines (*n*-butylamine and cysteamine) as well as the hydrolysis of the maleic anhydride moiety. Adduct formation is characterized via diagnostic IR stretches found within the fingerprint region, as well as via mass spectrometry, and provides insights towards the identity of the surface-formed product as well as valuable kinetic information. Two of the compounds expose terminal thiol and carboxylic acid groups, and as such we report on the improved adhesion to metal top contacts. The sum of these results show that this chemistry is effective in the installation of functionalities capable of improving metal adhesion for acene semiconductors.

Experimental

Maleic Anhydride Terminated Tetracene Thin Films

Precursor films (maleic anhydride terminated tetracene) were prepared following previously reported procedures.[87] Briefly, 50 nm of sublimed grade tetracene, (>99.99%) was deposited onto freshly prepared gold slides at a rate of 1 Å/s using a home built deposition chamber at a base pressure $< 3 \times 10^{-5}$ Torr. Thin films were terminated with maleic anhydride

by placing them in a Schlenk tube with 10 mg of source material, under nitrogen, for 48 h at 40 ºC, and non-chemisorbed materials were removed via vacuum.

Secondary Solid-State Reactions of Thin Films

Maleic anhydride terminated thin-films were placed in a drying chamber with a small vial containing the source material (~0.5 g of water or *n*-butylamine, 0.010 g of cysteamine). The drying chamber was then evacuated and filled with nitrogen three times and before it was sealed. The chamber was then placed in a furnace at 40 °C. Once the reaction was completed, the chamber was evacuated to less than 10^{-2} Torr and the base was cooled to -78 ºC to remove any vapors and physisorbed material on the film (1 h). Reactions of tetracene thin-films were examined, using a Bruker Optics Tensor 37 FT-IR with a polarization modulation accessory (PMA 50) and MCT detector.

Mass Spectrometry Analysis

Mass spectrometry samples were reacted under similar conditions described above, with the primary difference being the larger substrate size (75×25 mm). After secondary reaction and IR analysis, samples were then coated with CHCA matrix via a TM Sprayer from a stock solution of 5 mg/mL CHCA in 9:1 acetonitrile:water at 70 ºC with a flow rate of 0.100 mL/min. Coated samples were then examined with a Bruker Autoflex Speed MALDI-TOF in positive reflection mode. Prior to data acquisition, the instrument was calibrated to a peptide standard (Bruker Daltonik GmbH).

X-ray Photoelectron Spectroscopy Analysis

A Kratos AXIS-165 XPS was used to analyze cysteamine secondary reactions of precursor thin films. Photoelectrons were produced from a monochromatic Al X-ray source at an

incidence angle of 45° with a spot size of 200 µm and a chamber pressure of 3×10^{-10} Torr. All samples were referenced to C1s line at 284.6 eV.[94]

Solution Generated Reference Compounds

The solution generated maleic anhydride/tetracene adduct **(1)** was synthesized following a previous procedure.[88] Full synthetic methods and characterization for 5,12-dihydro-5,12-ethano-napthacene-15-*N*-butylpyrrolidine-14,16-dione **(2)**, *N*-butyl-5,12-dihydronapthacene-5,12-endo-α,β-succinamic acid **(2b)**, 5,12-dihydro-5,12-ethano-napthacene-13,14-dicarboxylic acid **(3)**, 5,12-dihydro-5,12-ethano-napthacene-15-*N*-(2-sulfanylethyl)pyrrolidine-14,16-dione **(4)** solution generated reference compounds are found in the Appendix B.

Adhesion Peel Tests

All preparations were identical except for the thickness of the starting tetracene thin film (100 nm). After precursor formation and secondary reaction, a thin film of Ag (50 nm) was thermally deposited onto the samples at a rate of 0.5 Å/s using a Kurt J. Lesker NANO 38 evaporator at a base pressure of $<1 \times 10^{-6}$ Torr. Metal adhesion was assessed by mounting samples to a support microscope slide, pressing Scotch® shipping/packing tape was pressed onto the surface, and peeled off at a peel angle of 180º three times. The films were imaged using a Hitachi SU3500 scanning electron microscope at up to 18000× magnification with accelerating voltages ranging from 4.00-5.00 kV.

Results and Discussion

SAMs are a viable and readily accessible way to alter surface properties of organic semiconductors. The solid/vapor Diels-Alder reactions have been shown to be successful under relatively mild conditions on pentacene, and simple molecules such as *N*-hydroxylmaleimide and maleic anhydride have been shown to reduce the hydrophobicity of the surface, reducing the

contact angle from 74º to 60º. The only caveat is that, due to factors such as vapor pressure and chemical incompatibility, dienophiles containing more device specific functionalities are difficult to react. Despite this, the Diels-Alder reacted precursor films provide an ideal site for further reactions as the anhydride moiety has an exceptional range of reactions and a wide variety of functional groups can be installed.[95] Of all possible secondary reaction, those utilizing primary amines or water are readily compatible with our vapor-solid reaction and have ample precedence in the solution phase.[96] With such reactions, the newly installed terminal functional group would provide a point at which coordination of metal clusters could occur, improving the overall adhesion between the tetracene film and the deposited metal, and thus mirroring the inorganic SAMs discussed in the introduction.

With the endpoint of adhesion in mind, our goals were threefold: to demonstrate secondary reactions, to produce materials that could not be made otherwise (e.g. thiols which were incompatible with the Diels-Alder chemistry), and to introduce functional groups to improve device properties, specifically adhesion. The first is most easily accomplished via the hydrolysis of the anhydride to form **2**. For the second, Diels-Alder reactions of thiol containing molecules are impractical due the intermolecular thiol-ene reaction and hence the reaction with cysteamine to form **3** would be compelling. Both reactions fulfill the third goal; the resultant carboxylic acid of **2** and thiol of **3** allows for the coordination of copper, silver, and gold top contacts.[90] The target reactions are summarized in Scheme 1.

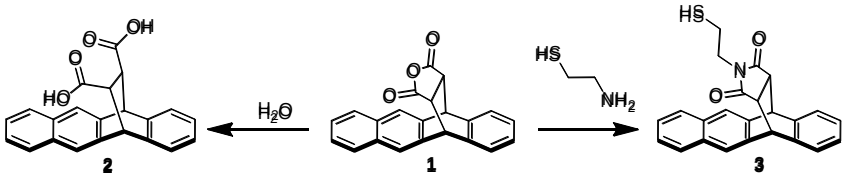

Scheme 1. Proposed secondary reactions of maleic anhydride functionalized tetracene thin-films.

Analysis of Secondary Reactions via PM-IRRAS

Secondary reactions of anhydride functionalized tetracene films was easily accomplished using only a drying chamber, sealed under nitrogen, in a furnace. Reaction progress was monitored via PM-IRRAS, an effective tool for thin-film characterization due to its surface selectivity and high sensitivity.[87] Product structure was determined by comparing surface spectra to solution-generated reference compounds, allowing for identification of newly formed stretches. For this process, we identified the most likely products based off classical organic reactivity; these solution-generated analogues were synthesized and characterized via ATR-IR. Distinct identifying IR stretches were selected for the reference compounds; in some cases, this was as many as 4 stretches, and all were unique within a window of $\geq$10 cm^{-1}. In all potential reaction products, the carbonyl frequencies were substantially distinct from the anhydride carbonyl, and served as a primary evaluation of both product identity and reaction progress.

To demonstrate the plausibility of secondary reactions, the hydrolysis of the anhydride was carried out to produce metal binding diacid species. Previous reactions conducted at 70 ºC indicated anhydride consumption, however the PM-IRRAS spectra contained abnormally broad which obscured product identity.[44] As temperature was suspected to affect the integrity of film and the surface species, and consequently the PM-IRRAS spectra, a lower temperature was chosen (40 ºC). Here, reactivity was significantly reduced. It was not until 48 h that full consumption of the carbonyl stretch of **1** at 1770 cm^{-1} (Figure 13a) was observed. During this time, the other stretches characteristic of the diacid **2** (1698, 1561, 1441, 1359, 1195, and 1135 cm^{-1}) were observed. These stretches also corresponded the identifying stretches of the solution generated reference (Appendix B), leaving little ambiguity to the identity of the reacted species.

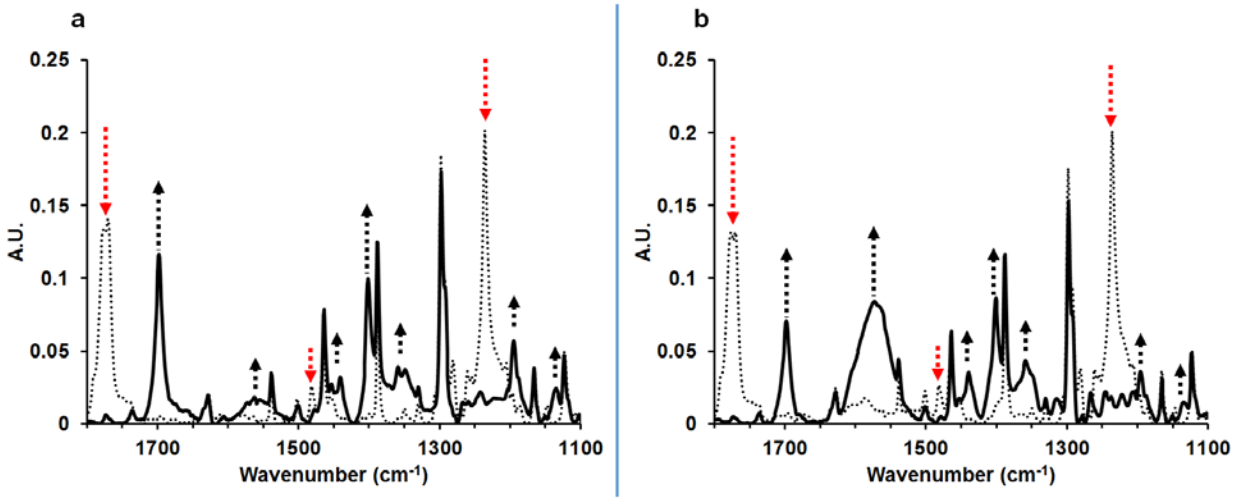

Figure 13. (a) PM-IRRAS spectra of the reaction of the anhydride functionalized tetracene thin-films (dotted line) with water (solid line) on the surface. Red arrows indicate the consumption of diagnostic stretches of **1** while black arrows indicate the production of **2**. (b) A similar hydrolysis reaction of **1** (dotted line) to form the diacid **2** (solid line). A larger broad stretch at 1561 cm^{-1}, along with a small carbonyl stretch at 1698 cm^{-1}, suggests the presence of hydrogen bonding.

One feature of the hydrolysis reaction that is worth mentioning is the broad but minor feature at 1561 cm^{-1}. In other samples, this feature was substantially larger (Figure 13b) and observed along with a dampening of the carbonyl stretch at 1698 cm^{-1}. We attribute this feature to hydrogen bonding in the reacted films, as typical diagnostic features, such as a shift in carbonyl frequencies along with the observation of stretch broadening,[97–99] are present. Typically, this occurs via one of two scenarios: in the first the diacid bonds with excess water present, in the second hydrogen bonding occurs intramolecularly. In order to investigate the former, the samples were exposed to vacuum (~5×10^{-6} Torr) for 2 h. A decrease in the stretch at 1561 cm^{-1} was not observed. The same is true for films placed in a P_2O_5 desiccator for several days. Thus we believe the most likely explanation for this phenomenon is intramolecular hydrogen bonding, which is common for maleic acid and other analogues.[99–102]

Despite the success of the hydrolysis reaction there were some concerns about the modest reactivity and the exposure of organic semiconductor films to water is generally undesirable.[103]

Accordingly, we shifted focus to imide formation, and the eventual reaction of cysteamine. To demonstrate the viability of amine secondary reactions, anhydride SAMs were first exposed to *n*-butylamine vapors. Imide formation is a rapid reaction, and the high vapor pressure of *n*-butylamine[104] assures that sufficient amounts of the reactants reach the surface. After 18 h of exposure, complete consumption of the anhydride's carbonyl stretch at 1770 cm^{-1} was observed along with the consumption of other diagnostic stretches (red arrows, Figure 14). At the same time, the production of new stretches at 1696, 1436, 1395, and 1354 cm^{-1} were observed. These were found to match the IR spectra of the solution generated reference *n*-butylmaleimide/tetracene adduct (**4**, Appendix B), which confirmed the presence of this species on the thin-film surface. It should be noted that a minor stretch at 1562 cm^{-1} is only found in the *n*-butylmaleamic acid adduct (**4b**, Appendix B), however other diagnostic stretches are not observed and we assume that if **4b** is present, it is a minor side product. With the production of **4** confirmed, baseline kinetics for imide formation were established to aid with subsequent amine reactions (i.e. cysteamine). Overall the reaction was quite rapid. It was found that complete consumption of anhydride stretch of **1** was observed in as little as 30 min, even at a reduced temperature (30 °C). Further reduction in reaction time would likely begin to involve the kinetics of the vapor transport, and no further attempts were made to study this effect.

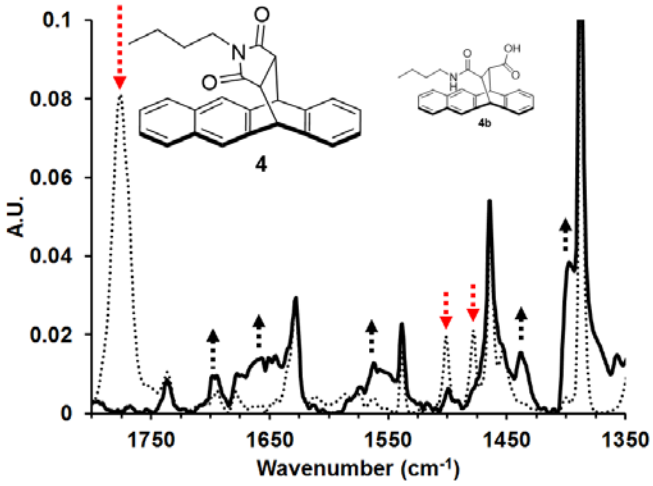

Figure 14. PM-IRRAS spectra of the reaction of the anhydride functionalized tetracene thin-films (dotted line) with *n*-butylamine (solid line) on the surface. Red arrows indicate the consumption of diagnostic stretches of **1** while black arrows indicate the production of **4** and **4b**.

For the final reaction, anhydride functionalized tetracene thin-films were exposed to cysteamine vapor at 40 °C. Similar to the *n*-butylamine, full consumption of the anhydride stretches occurs rapidly (1 h, Figure 15), however interpretation of new stretches is challenging. Due to overlap with tetracene signals, only 2 new distinct signals are found. Of these two, the stretch at 1264 cm^{-1} does correspond to the solution-generated reference imide **3**; the other broad stretch at 1572 cm^{-1} is not present in the reference imide IR spectra (Appendix B), nor has it been present in the unpurified reference of the acid amide. The IR spectra shown in Figure 4 is representative of multiple attempts, and in all instances, additional identifiable peaks are absent. A second method is necessary for identification and could also be a useful complementary characterization for the previous reactions.

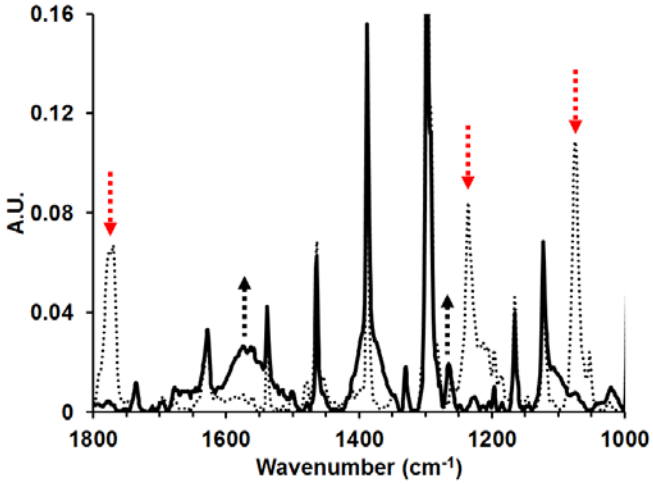

Figure 15. PM-IRRAS spectra of the secondary reaction of the anhydride functionalized thin-films (dotted line) with cysteamine. The spectra post reaction (solid line) is inconclusive for the identity of the product.

Analysis of Cysteamine-Reacted Thin-films via MALDI-TOF and XPS

For the secondary reactions performed on the thin-films, interpretation of product PM-IRRAS spectra can be challenging due to the absence of a few diagnostic stretches because of factors such as the surface selection rule.[63] Additionally, different regioisomers are possible at the surface, possibly contributing to broad and unexpected stretches, which obfuscates analysis. Finally, reaction with *n*-butylamine suggest that both the imide and acid amide might be present. Thus, a second method of analysis becomes important in identifying reaction product formed with amines. Previously, identification of SAMs on *inorganic* surfaces have been achieved using matrix assisted laser desorption ionization time of flight (MALDI-TOF) mass spectrometry.[91] Adapting this technique for use on organic thin-films would greatly improve our confidence in product identity.

After optimizing the technique on several controls including solution generated reference compounds and references physically deposited on top of tetracene thin-films, the cysteamine reacted sample was examined. Interestingly, the molecular ions of neither the imide **3** nor the

acid-amide **3b** products are observed via MALDI-TOF analysis. Other viable product structures were then screened, and instead, the imide and acid-amide containing the disulfide (**3c** and **3d**) were identified (Figure 16). This was surprising, despite the fact that the disulfide is a common degradant of cysteamine, as the vapor pressure of the disulfide (cystamine) was expected to be much lower than that of cysteamine. Thus, we sought to elucidate the plausibility of the disulfide entering the vapor phase and reacting with the precursor films. The reaction of the anhydride functionalized films with pure disulfide demonstrated that the anhydride was consumed at a slightly lower rate than the cysteamine (2 h vs 1 h, respectively, 50º), but indeed did react. Overall this pathway is viable, but due it's the slower kinetics, we suggest the dominant mechanism is cysteamine reacting with the anhydride on the surface first, and that the thiol is converted to the disulfide over time. Finally, we should note that the lack of **3** and **3b** in the MALDI spectrum can be attributed to the absence of these species on the surface; the reference imide compound **3** was readily observed when directly mounted on a slide.

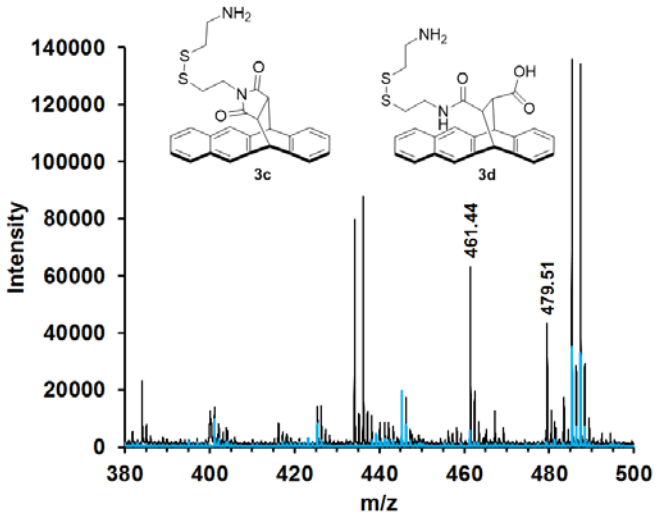

Figure 16. MALDI-TOF spectra of a cysteamine reacted thin film (black) compared to CHCA matrix only (blue). $[M+H]^+$ ions of **3c** and **3d** are highlighted.

A concern with relying exclusively on mass spectrometry data is the highly variable ionization efficiency between compounds, and thus the possibility of unrepresentative identification. Complimentary assessment with X-ray photoelectron spectroscopy (XPS), which is particularly effective at elemental and chemical analysis, provides a fuller picture of the formed products. As only the top ~10 nm of the film produces photoelections that can be detected,[105] XPS results in characterization of the film's surface without interference of the bulk signal. XPS was utilized on a cysteamine reacted sample. Deconvolution of the O 1s signal (Figure 17a) indicates the presence of two peaks. The higher binding energy at 532.1 eV has been attributed to carbonyl oxygen. Carboxylates are commonly found at ~1 eV lower binding energy and thus it is highly likely the signal at 531.1 eV is due to this functionality.[106] Signal integration of these two components indicate that 22% of the surface species is from a carboxylate while the remainder is a carbonyl. In a similar manner, deconvolution of the N 1s region yielded two peaks (Figure 17b). The first, with a binding energy of 399.8 eV is typical of amide and imide nitrogens,[107] and as such the relative abundance of each species cannot be determined. The second peak at a binding energy of 401.3 eV, however, has been attributed to charged amide from proton transfer and/or hydrogen bonding.[107,108] Signal integration of the two peaks yielded a ratio of 1.4:1, indicating that 41% of the surface species are charged. Taken together the N 1s and O 1s signals are suggestive of hydrogen boding between the carboxylic acid and amide in **3d**. If we assume that nearly all the acid-amide is hydrogen bonding, this would indicate that roughly 40% of surface species are of this form, while the remainder are the imide **3c**. This is consistent with the MALDI data as well. The finding of hydrogen bonding could also explain the stretch broadening observed in the PM-IRRAS spectra.

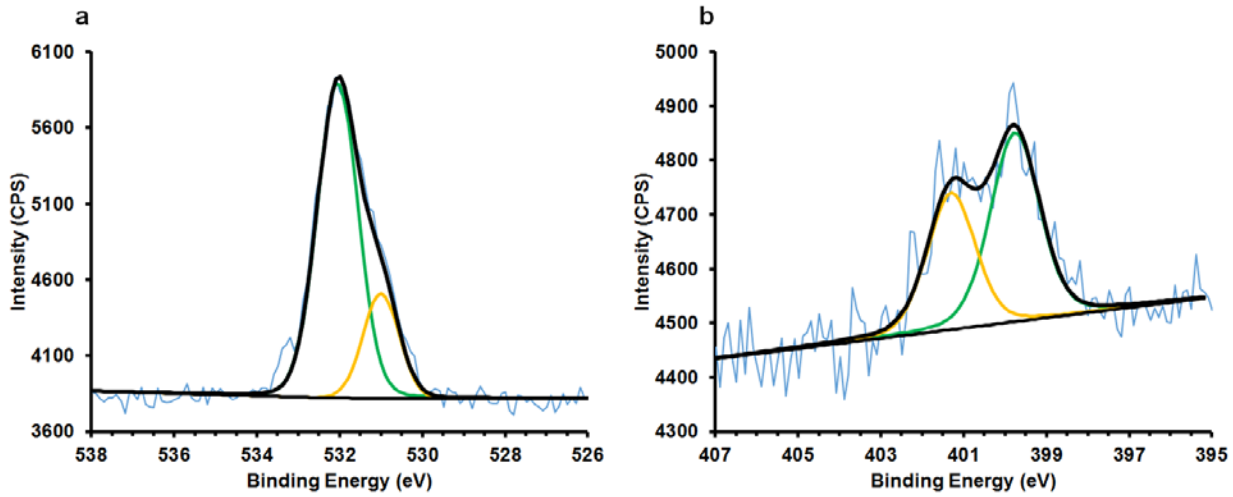

Figure 17. Deconvoluted XPS spectra of (a) O 1s and (b) N 1s obtained from a cysteamine reacted thin-film. The green peaks are attributed to the neutral species while the peaks in yellow are assigned to charged/hydrogen bonded species. All peaks are reference to C 1s of 284.6 eV.

Adhesion Tests of Cysteamine Reacted Films

As a standard qualitative measure of adhesion,[109] peel tests using Scotch® packing tape were performed on the unreacted tetracene and the secondary cysteamine reacted thin-films. Before the tape was applied to the films, silver (50 nm) was deposited onto the films. Upon application of the tape to the samples and peeling back, a noticeable loss of silver on the unreacted tetracene sample (Figure 18a) was observed. The cysteamine reacted film, in contrast, proved to be more robust (Figure 18b). SEM analysis further illustrates these improvements. Film structure in Figure 18a is heavily damaged even in a manner consistent with macroscopic observations; areas where the silver contact appears slightly discolored indeed contain flaws. Areas that appear unperturbed (left of SEM image) still contain significant pitting if not holes. In contrast, the reacted surface contain virtually no flaws at this or higher magnification (up to 18000×). It is quite clear that the reaction has improved adhesion. Importantly, the improved adhesion continues with the other reactions as the silver layer was unable to be removed from thin films containing the diacid **2**. We further confirmed the role of the terminal group by

examining **4,** which lacks a terminal metal binding group. As expected this functionalization did not improve the overall adhesion of the contact. Overall, the peel tests are indicate that metal coordinating functionalities installed via secondary reactions improve adhesion between a deposited metal and an organic film.

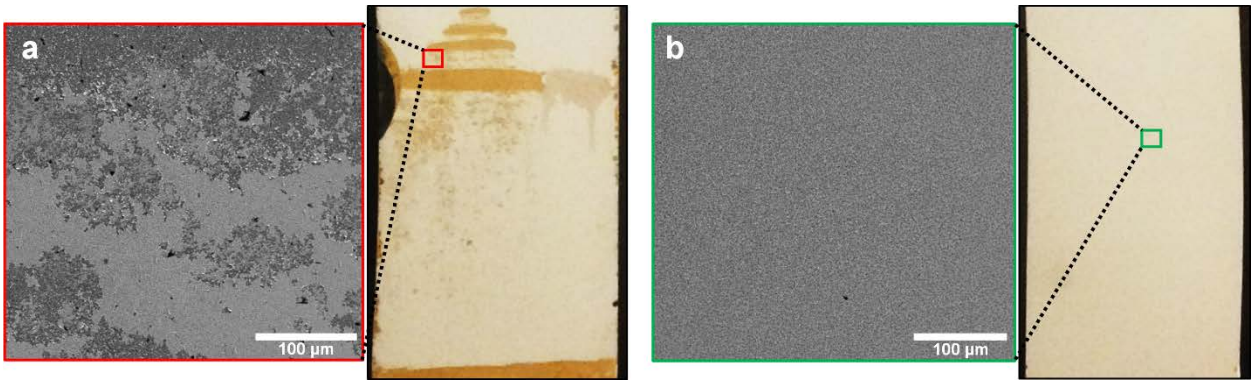

Figure 18. Peel tests of metalized thin films of tetracene (a) and cysteamine reacted tetracene (b). SEM imaging shows the features as a result of the removal of silver (red box) contrasted to the surface of the cysteamine reacted film (green box).

Conclusion

With the goal of improving metal adhesion for organic semiconductor thin films, secondary reactions were performed on anhydride functionalized tetracene thin films. Reactions were monitored via IR spectroscopy through the consumption of the surface anhydride species and the generated stretches were compared to solution generated references of the most likely products. Due to the complexity of the IR spectra for the cysteamine reaction, additional analysis was performed on the films using MALDI-TOF mass spectrometry and XPS, which suggests the presence of a dimer of the anticipated imide formed via a disulfide linkage. Peel tests revealed that improved adhesion on metalized secondary reacted films; silver was easily delaminated from tetracene, while reacted films showed no peel damage. The results from the peel tests also confirms the necessity of metal coordinating species on the functionalized organic

thin films. Combined, these results demonstrate a direct way to address adhesion and other interfacial flaw within organic devices and allow surface functionalities to be tuned for said purposes.

APPENDIX A

SUPPLEMENTAL INFORMATION FOR CHAPTER TWO

General Experimental Methods:

All reactions were run under a nitrogen atmosphere unless otherwise stated. All column chromatography separations were performed on silica gel 60 (40-63 μm from BDH). Thin layer chromatography was carried out on silica gel (F_{254}) with glass support. All NMR spectra were taken on a Varian 500 MHz spectrometer. All ^{1}H and ^{13}C chemical shifts (δ) were referenced to tetramethylsilane in $CDCl_3$. IR spectra were acquired on a Shimadzu IRAffinity-1S FTIR with a Pike Technologies MIRacle single reflection horizontal ATR accessory. Mass spectra were acquired on a Shimadzu ESI-TOF. Dimethyl spiro[cycloprop[2]ene-1,9′-fluorene]-2,3-dicarboxylate was prepared following a previous procedure.[60]

Synthesis of DHI-9:

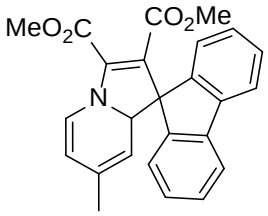

7′-Methyl-8a′*H*-spiro[fluorine-9,1′-indolizine]-2′,3′-dicarboxilate (DHI-9): 4-Methylpyridine (0.010 g, 0.11 mmol) and dimethyl spiro[cycloprop[2]ene-1,9′-fluorene]-2,3-dicarboxylate (0.037 g, 0.12 mmol) were added to a round bottomed flask. The flask was evacuated and filled with nitrogen (×3). Dichloromethane (2 mL) was added to the flask and the solution was stirred in the dark for 4 h. The product (0.028 g, 0.069 mmol) was purified via column chromatography (100% DCM, R_f = 0.38) and collected as a green oil at a 65% yield. ^{1}H NMR (500 MHz) δ 7.72 (d, *J* = 7.3 Hz, 2H), 7.56 (d, *J* = 7.3 Hz, 1H), 7.46 (d, *J* = 7.6 Hz, 1H), 7.40-7.29 (m, 3H), 7.22 (t, *J* = 7.4 Hz, 1H), 6.40 (d, *J* = 7.3 Hz, 1H), 5.43 (s, 1H), 5.06 (dd, *J* = 7.5, 1.1 Hz, 1H), 4.19 (s, 1H), 3.99 (s, 3H), 3.26 (s, 3H), 1.51 (s, 3H). ^{13}C NMR (125 MHz) δ 163.6, 162.1, 147.3, 146.5, 142.5, 141.5, 140.1, 131.5, 128.0, 127.8, 127.3, 126.8, 124.6, 123.7, 123.3, 119.7, 119.4, 112.5, 108.6, 108.2, 69.9, 64.2, 53.1, 50.9, 20.6. IR (ATR, cm^{-1}): 2949, 2789, 1742, 1694, 1649, 1593, 1557, 1460, 1435, 1393, 1308, 1263, 1225, 1182, 1130, 1084, 731. HRMS (ESI-TOF) m/z: $[M + H]^+$ Calcd for $C_{25}H_{21}NO_4H$ 400.1504; Found 400.1525.

Figure S1. Solution UV-vis of **DHI-1**, **6**, and **14** half-life data

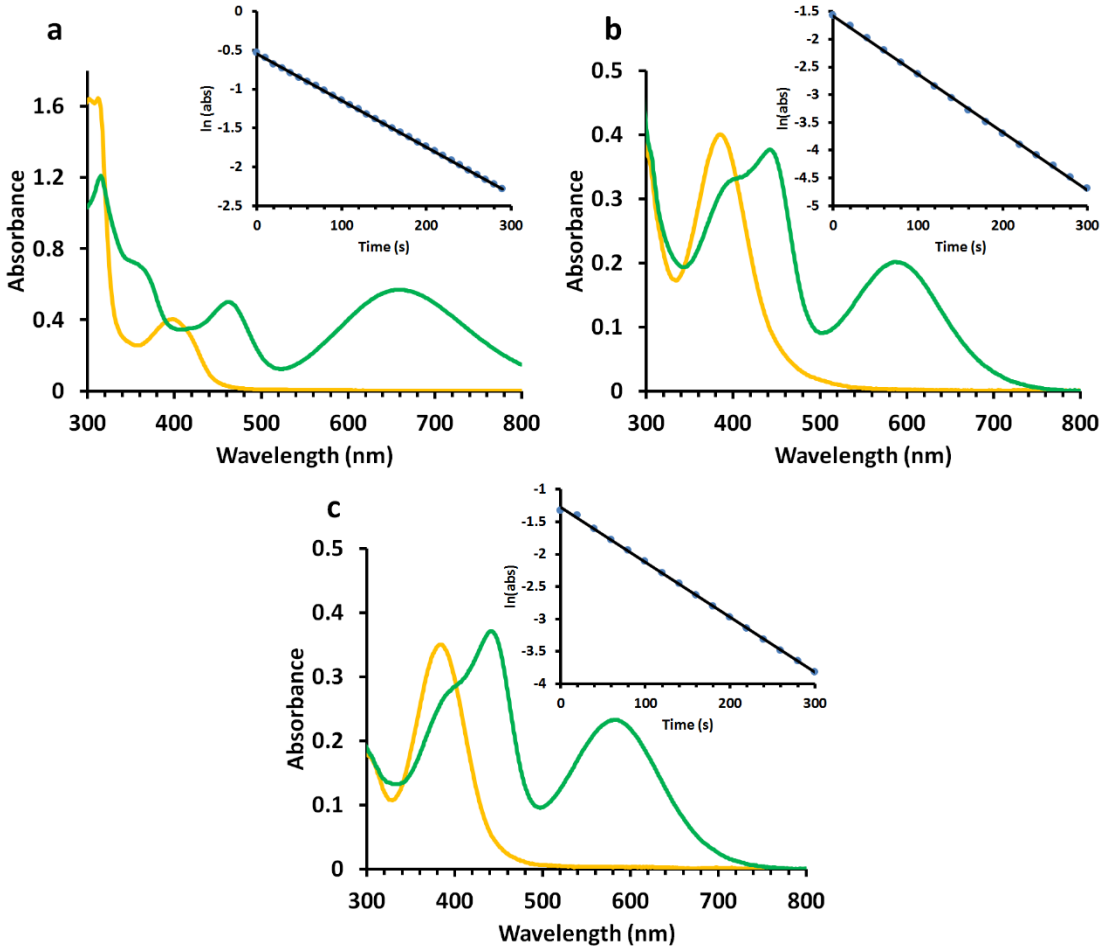

Optical of properties of (a) **DHI-1** (7.0×10^{-5} M), (b) **6** (6.9×10^{-5} M), and (c) **14** (7.0×10^{-5} M) were studied via solution (dichloromethane) UV-vis. In the spiro form (yellow), the typical π-π* transition can be observed at 397, 385, and 386 nm respectively. Upon irradiation with 400 nm light for 2 minutes (green), the presumed charge transfer band is observed at 657, 586, and 602 nm respectively. Half-lives (insets) were found to be 115, 66, and 47 seconds respectively and followed predicted first order rate.

Figure S2. PM-IRRAS spectra for DHI thin-films

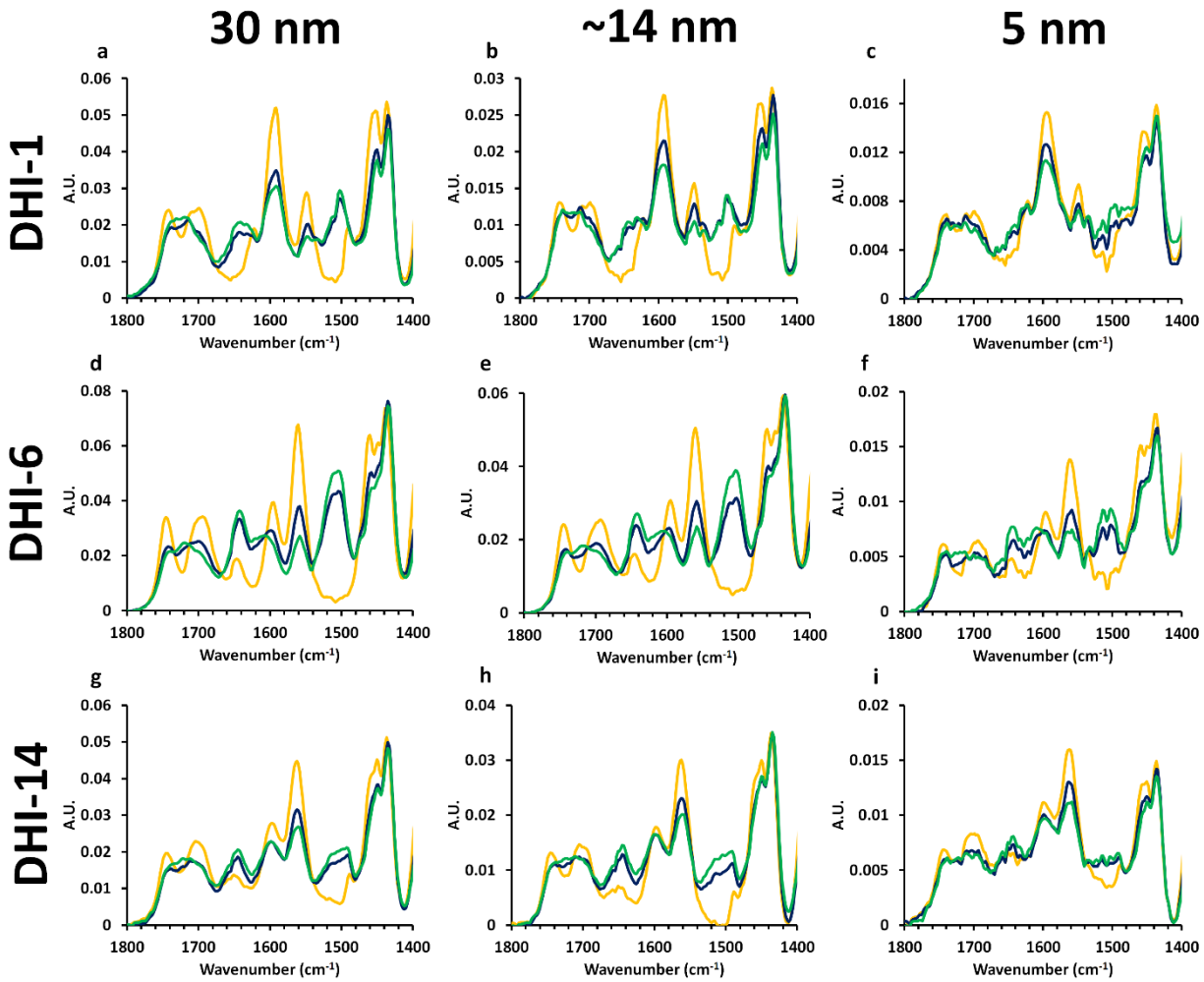

DHI-1 (**a-c**), **6** (**d-f**), and **14** (**g-i**) spiro (yellow) thin-films were irradiated with 400 nm light for 2 (blue) and 8 minutes (green). Consumption of the stretch at 1560 cm^{-1} along with the growth of the stretch at 1500 cm^{-1} indicates successful photoconversion.

Figure S3. PM-IRRAS spectra of **DHI-9**

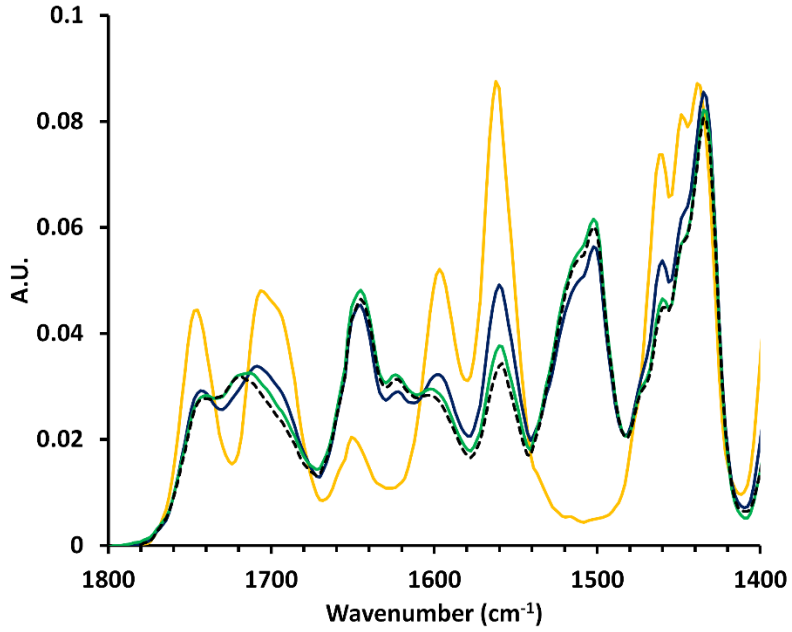

Representative spectra for **DHI-9** thin-films. The spiro (yellow) film was irradiated with 400 nm light for 2 (blue), 8 (green), and 13 (black dotted) minutes. The consumption of the stretch at 1560 cm^{-1} along with the growth of the stretch at 1500 cm^{-1}, indicates successful photoconversion.

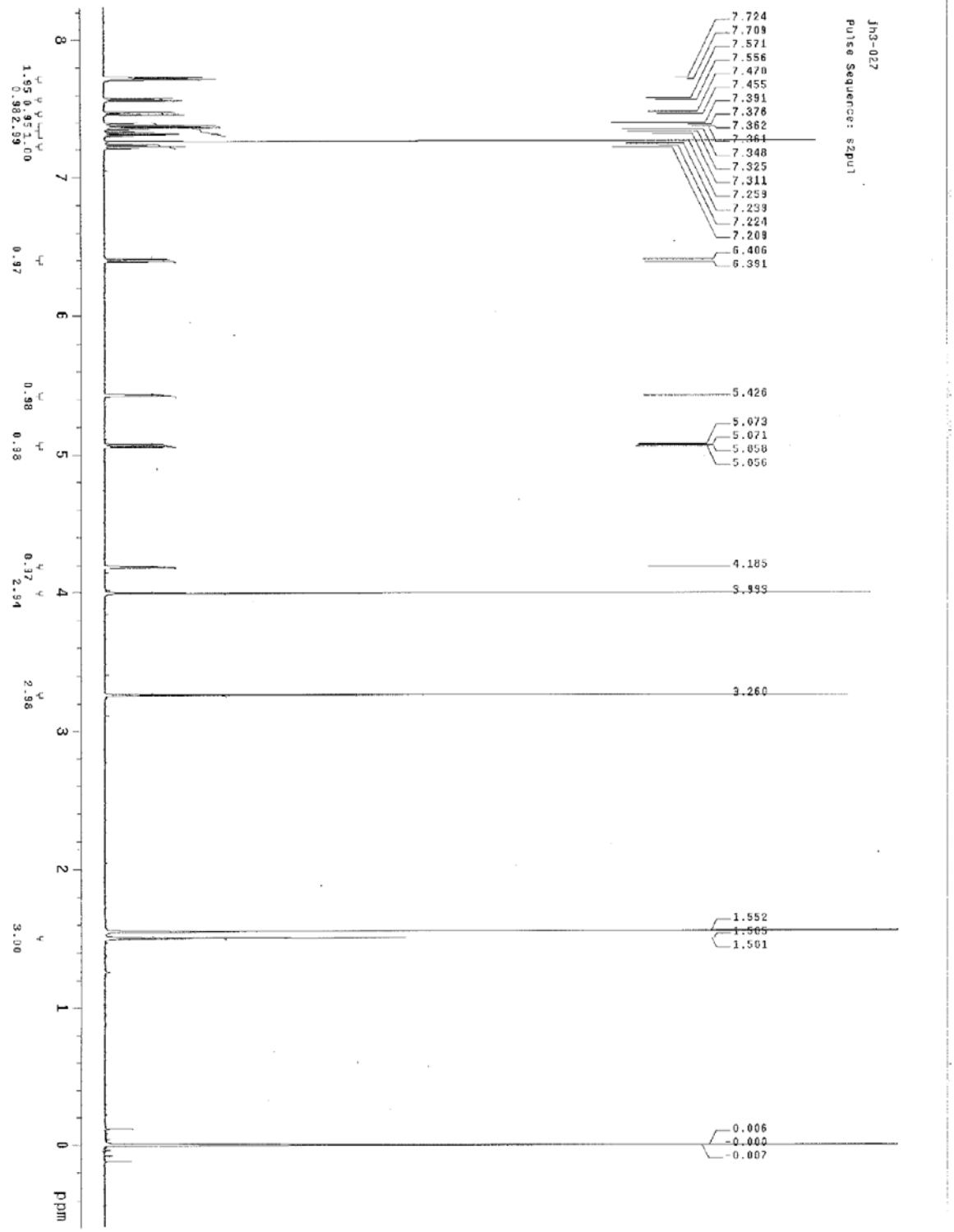
jh3-027
Pulse Sequence: s2pul
7.724
7.709
7.571
7.556
7.470
7.455
7.391
7.376
7.362
7.361
7.348
7.325
7.311
7.259
7.239
7.224
7.209
6.406
6.391
5.420
5.073
5.071
5.058
5.056
4.185
3.993
3.260
1.552
1.505
1.501
0.006
-0.000
-0.007
ppm

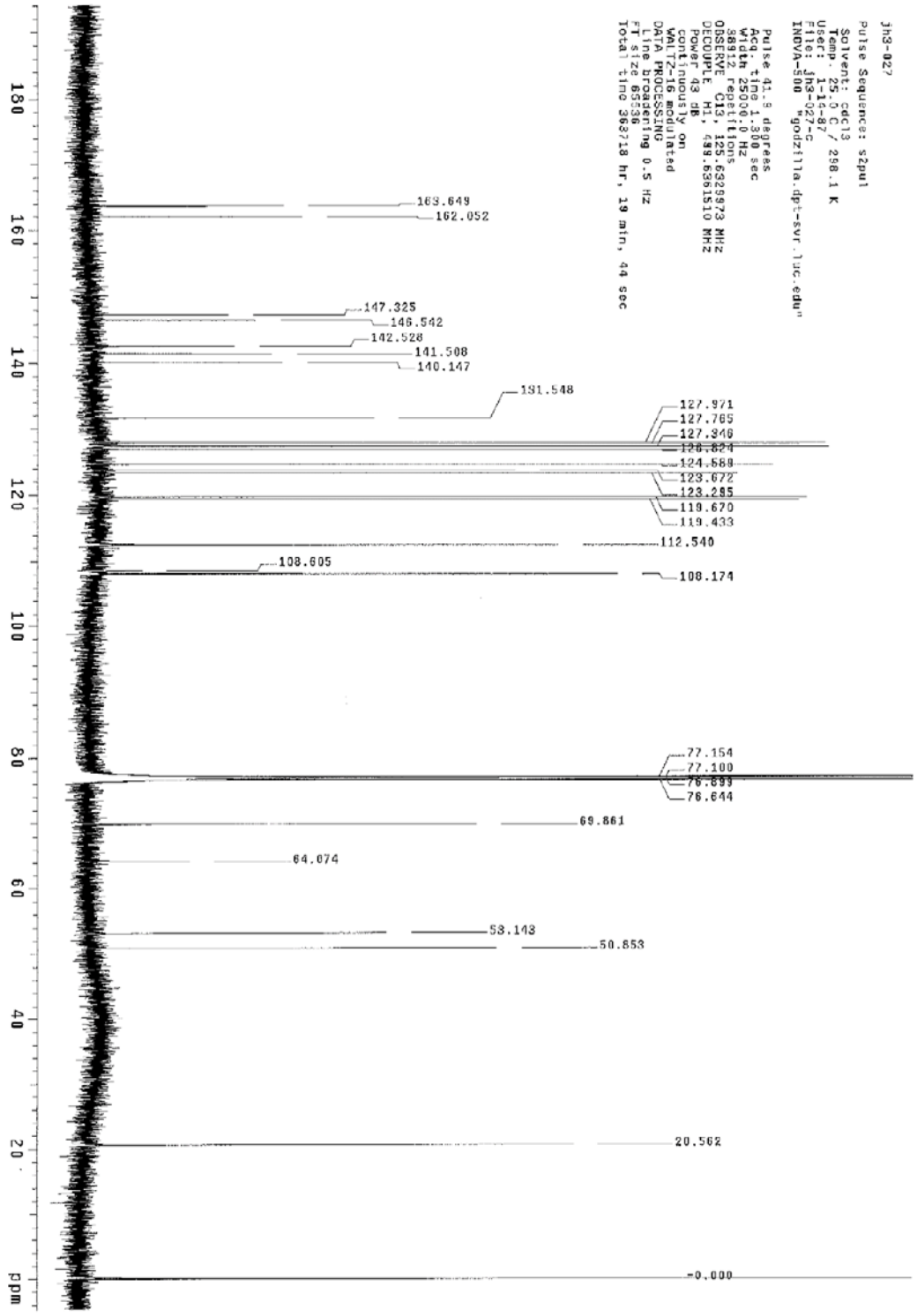
jh3-027
Pulse Sequence: s2pul
Solvent: cdcl3
Temp. 25.0 C / 298.1 K
User: 1-16-87
File: jh3-027-c
INOVA-500 "godzilla.dpt-svr.luc.edu"
Pulse 41.5 degrees
Acq. time 1.300 sec
Width 25000.0 Hz
38912 repetitions
OBSERVE C13, 125.6329973 MHz
DECOUPLE H1, 499.8361510 MHz
Power 43 dB
continuously on
WALTZ-16 modulated
DATA PROCESSING
Line broadening 0.5 Hz
FT size 65536
Total time 36218 hr, 19 min, 44 sec
169.649
162.052
147.325
146.542
142.528
141.508
140.147
131.548
127.971
127.765
127.346
126.824
124.588
123.672
123.285
119.670
119.433
112.540
108.605
108.174
77.154
77.100
76.699
76.644
69.861
64.074
53.143
50.853
20.562
-0.000
ppm

APPENDIX B

SUPPLEMENTAL INFORMATION FOR CHAPTER THREE

General Experimental Methods:

All reactions were run under a nitrogen atmosphere and solvents were purged unless otherwise stated. All column chromatography separations were performed on silica gel 60 (40-63 μm from BDH). Thin layer chromatography was carried out on silica gel (F_{254}) with glass support. All NMR spectra were taken on a Varian 500 MHz spectrometer. ^{1}H and ^{13}C chemical shifts (δ) in $CDCl_3$ were referenced to tetramethylsilane. ^{1}H and ^{13}C chemical shifts (δ) in DMSO-d_6 were referenced to its residual solvent signal (2.50 and 39.51 respectively).[110] IR spectra were acquired on a Shimadzu IRAffinity-1S FTIR with a Pike Technologies MIRacle single reflection horizontal ATR accessory. 5,12-Dihydro-5,12-ethano-napthacene-13,14-dicarboxylic acid anhydride (maleic anhydride adduct, **1**) was synthesized using a previous procedure.[88]

Synthetic Methods

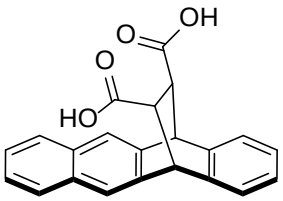

5,12-Dihydro-5,12-ethano-napthacene-13,14-dicarboxylic acid (2): 5,12-Dihydro-5,12-ethano-napthacene-13,14-dicarboxylic acid anhydride (0.0329 g, 0.101 mmol) was added to a sealed tube which was evacuated and filled with nitrogen three times. Water (0.5 mL, 27.7 mmol) and THF (1 mL) were added to the tube which was sealed and placed in an oil bath at 70 °C. After 43 h, the tube was removed from the oil bath and cooled to room temperature. The solvent was then removed and CH_2Cl_2 added to form a white precipitate that was collected via vacuum filtration. This yielded the desired diacid as white powder (0.0129 g, 0.0374 mmol, 37 %) as a single isomer. ^{1}H NMR (500 MHz, DMSO-d_6) δ 12.04 (s, 2H), 7.84-7.80 (m, 4H), 7.44 (dd, J = 6.2, 3.3 Hz, 2H), 7.30 (dd, J = 5.3, 3.3 Hz, 2H), 7.07 (dd, J = 5.4, 3.2 Hz, 2H), 4.69 (s, 2H), 3.17 (s, 2H). ^{13}C NMR (125 MHz, DMSO-d_6) δ 172.4, 140.9, 140.5, 131.6, 127.3, 125.41, 125.36, 124.9, 121.1, 47.3, 46.3. IR (cm^{-1}) 1713, 1501, 1479, 1414, 1315, 1227, 1207, 889, 748, 673.

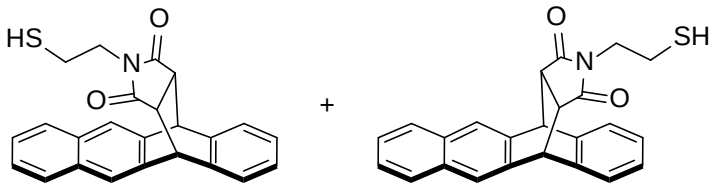

5,12-Dihydro-5,12-ethano-napthacene-15-*N*-(2-sulfanylethyl)pyrrolidine-14,16-dione (3): Open to the air, 5,12-dihydro-5,12-ethano-napthacene-13,14-dicarboxylic acid anhydride (0.1204 g, 0.3689 mmol), cysteamine (0.0380 g, 0.492 mmol), and acetic acid (5 mL) were added to a

round bottom flask. The mixture was then refluxed for 8.5 h and then cooled to room temperature. The mixture was then poured into water (10 mL) to form a white precipitate. The powder was collected via vacuum filtration and rinsed with water three times. The product was dried overnight, which provided 0.1092 g (0.2847 mmol) of **3** in 77%. Major Isomer: ^{1}H NMR (500 MHz, $CDCl_3$) δ 7.81-7.78 (m, 4H), 7.46 (dd, *J* = 6.1, 3.2 Hz, 2H), 7.32 (dd, *J* = 5.4, 3.4 Hz, 2H), 7.17 (dd, *J* = 5.4, 2.9 Hz, 2H), 4.91 (s, 2H), 3.34-3.28 (m, 4H), 1.88 (q, *J* = 7.8 Hz, 2H), 1.04 (t, *J* = 9.3 Hz, 1H). ^{13}C NMR (125 MHz, $CDCl_3$) δ 176.2, 138.3, 132.2, 127.2, 126.0, 125.0, 124.2, 122.5, 46.6, 45.4, 41.4, 20.8. Minor Isomer: ^{1}H NMR (500 MHz, $CDCl_3$) δ 7.74 (dd, *J* = 5.9, 3.4 Hz, 2H), 7.72 (s, 2H), 7.44-7.41 (m, 4H), 7.20 (dd, *J* = 5.4, 2.9 Hz, 2H), 4.90 (s, 2H), 3.34-3.28 (m, 2H), 3.19 (t, *J* = 7.6 Hz, 2H), 1.64-1.58 (m, 2H), 0.68 (t, *J* = 8.5 Hz, 1H). ^{13}C NMR (125 MHz, $CDCl_3$) δ 176.3, 140.9, 138.2, 135.7, 132.2, 127.4, 126.9, 126.1, 123.4, 46.8, 45.4, 41.2, 20.5. IR (cm^{-1}) 1771, 1695, 1437, 1395, 1337, 1260, 1155, 893, 847, 764.

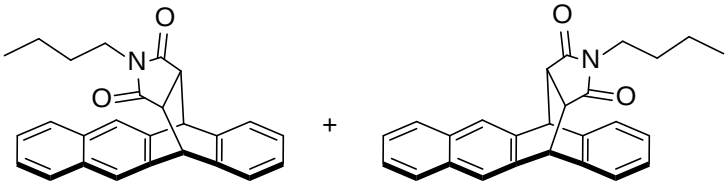

5,12-Dihydro-5,12-ethano-napthacene-15-*N*-butylpyrrolidine-14,16-dione (4): Tetracene (0.0448 g, 0.196 mmol) and *n*-butylmaleimide (0.0399 g, 0.260 mmol) were added to a tube which was evacuated and filled with nitrogen three times. Toluene (2 mL) was then added to the tube, which was then sealed and placed in an oil bath at 120 °C. After 48 h, the reaction was cooled to room temperature and the solvent was removed. The crude product was purified via column chromatography (1:4 EtOAc: hexanes, R_f: 0.48) to yield the it as a white powder (0.0325 g, 0.0843 mmol) at a 43% yield. Two inseparable isomers: ^{1}H NMR (500 MHz, $CDCl_3$) δ 7.80-7.78 (m, 4H), 7.74-7.71 (m, 4H), 7.45 (dd, *J* = 6.1, 3.2 Hz, 2H), 7.42-7.39 (m, 4H), 7.31 (dd, *J* = 5.4, 3.4 Hz, 2H), 7.19 (dd, *J* = 5.6, 3.2 Hz, 2H), 7.14 (dd, *J* = 5.4, 2.9 Hz, 2H), 4.91-4.88 (m, 4H), 3.27-3.25 (m, 4H), 3.13 (t, *J* = 7.1 Hz, 2H), 3.02 (t, *J* = 6.8 Hz, 2H), 0.84-0.79 (m, 4H), 0.71 (t, *J* = 6.6 Hz 3H), 0.42-0.34 (m, 4H), 0.11 (t, *J* = 6.8 Hz, 3H). ^{13}C NMR (125 MHz, $CDCl_3$) δ 176.7, 176.6, 141.1, 138.7, 138.2, 135.8, 132.4, 132.2, 127.49, 127.47, 127.0, 126.8, 125.9, 125.8, 125.0, 124.2, 123.4, 122.4, 46.8, 46.6, 45.4 (2), 38.4, 38.3, 29.2, 29.1, 19.7, 19.4, 13.6, 12.8. IR (cm^{-1}) 1695, 1460, 1435, 1398, 1341, 1292, 1192, 1132, 935, 897, 849, 754, 721.

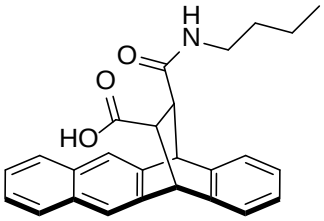

***N*-butyl-5,12-dihydronapthacene-5,12-endo-α,β-succinamic acid (4b):** 5,12-Dihydro-5,12-ethano-napthacene-13,14-dicarboxylic acid anhydride (0.0565 g, 0.173 mmol) was dissolved in CH_2Cl_2 (2 mL) and cooled to 0 °C. To the resulting suspension, *N*-butylamine (0.03 mL, 0.3 mmol)

in CH_2Cl_2 (0.1 mL) was added dropwise. The mixture was then stirred at 0 °C for 3 h and then brought to room temperature. The pH of the solution was adjusted to 10 with 1 M NaOH and extracted with water (×3). The pH of the combined aqueous layers was adjusted to 4 with 1 M HCl, which resulted in a white precipitate that was vacuum filtered. The crude product was triturated with toluene, yielding a white powder that was collected via vacuum filtration. This produced the desired product **4b** (0.0164 g, 0.0415 mmol) in 24% yield. ^{1}H NMR (500 MHz, DMSO-d_6) δ 7.85-7.77 (m, 5H), 7.42 (dd, J = 6.1, 3.2 Hz, 2H), 7.32 (d, J = 6.8 Hz, 1H), 7.11 (d, J = 6.4 Hz, 1H), 7.05 (t, J = 6.6 Hz, 1H) 7.00 (t, J = 6.8 Hz, 1H), 4.63 (d, J = 1.5 Hz, 1H), 4.50 (d, J = 2.5 Hz, 1H), 3.22 (dd, J = 10.7, 2.4 Hz, 1H), 2.99-2.83 (m, 3H), 1.37-1.26 (m, 4H), 0.86 (t, J = 7.1 Hz, 3H). ^{13}C NMR (125 MHz, DMSO-d_6) δ 172.5, 169.6, 141.7, 140.84, 140.81, 140.5, 131.51, 131.49, 127.3, 127.2, 125.37, 125.35, 125.33, 125.1, 125.0, 124.4, 121.2, 120.8, 47.9, 47.5, 46.7, 45.1, 38.1, 31.2, 19.5, 13.7. IR (cm^{-1}) 1711, 1670, 1643, 1562, 1437, 1381, 1321, 1256, 1207, 1165, 947, 881, 687, 665.

Figure S4. ATR-FTIR spectra of **2**.

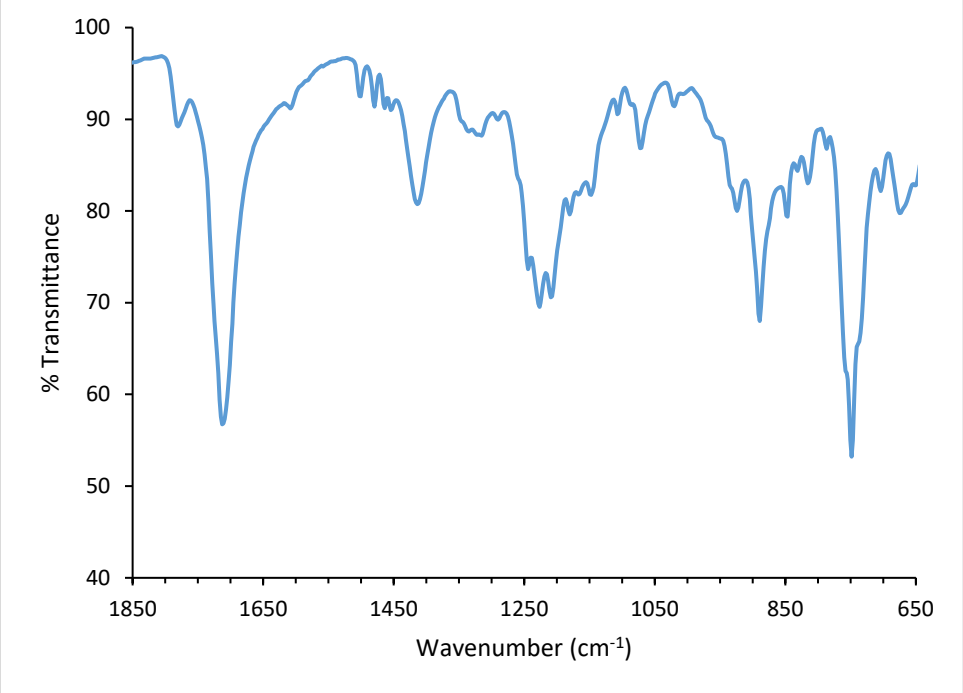

Figure S5. ATR-FTIR spectra of **3**.

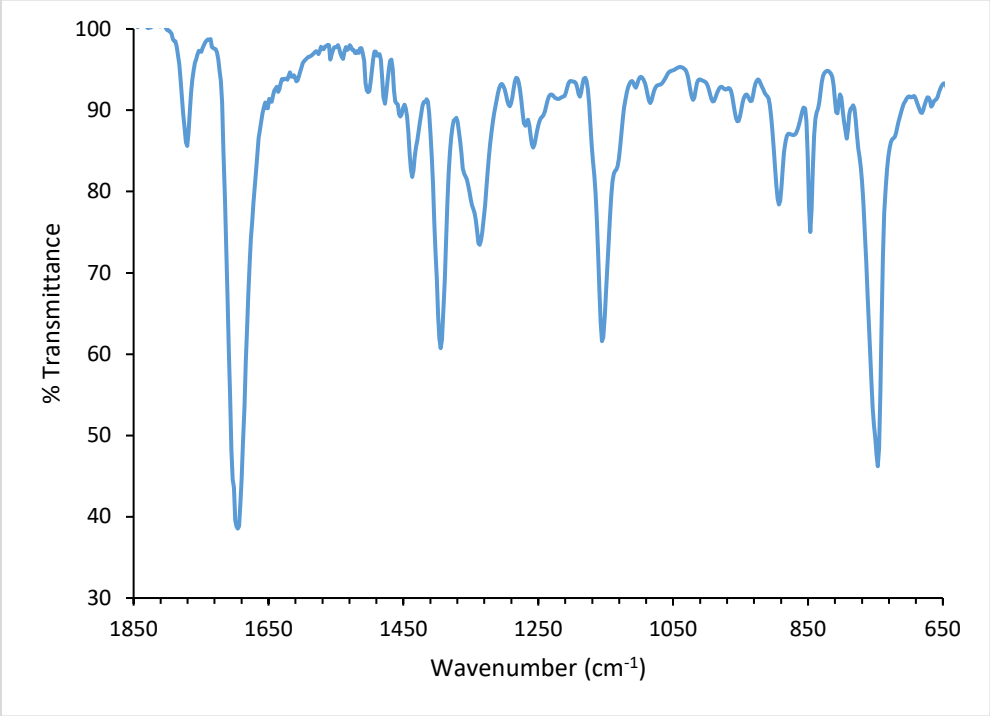

Figure S6. ATR-FTIR spectra of **4**.

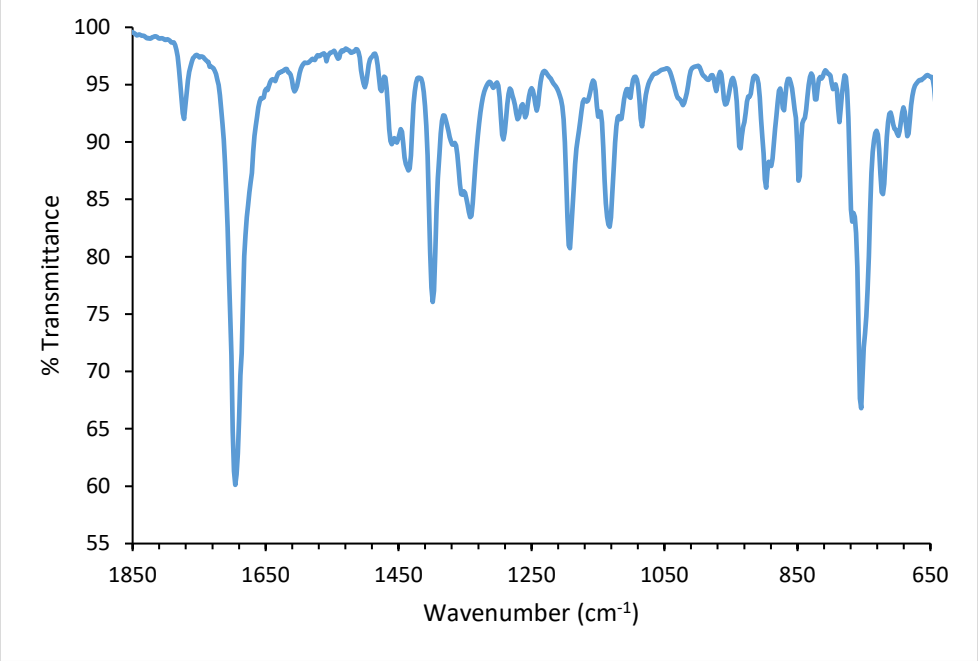

Figure S7. ATR-FTIR spectra of **4b**.

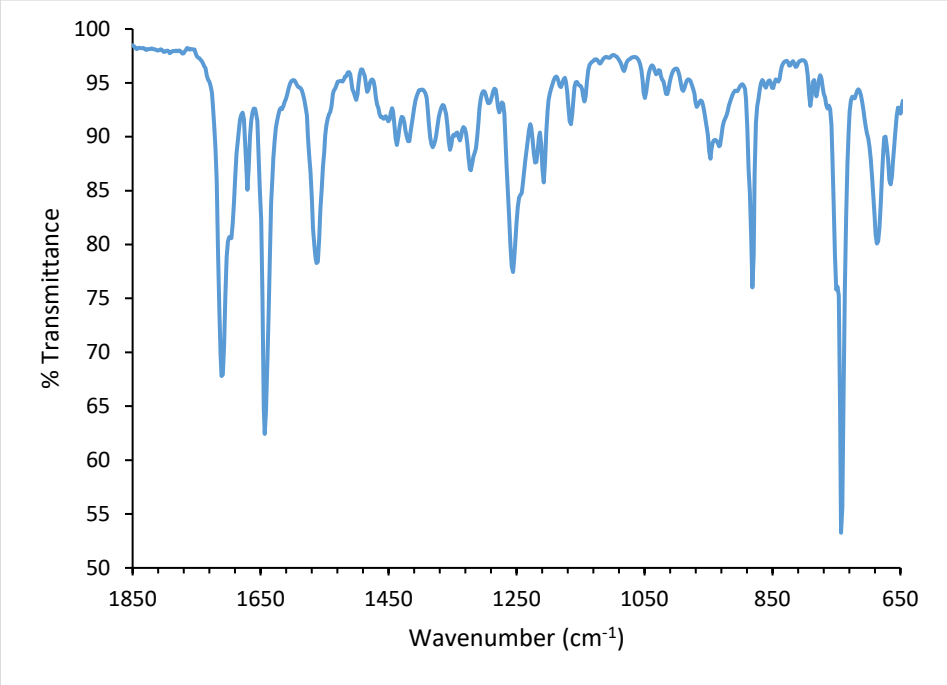

REFERENCE LIST

(1) Du, X.; Durgan, C. J.; Matthews, D. J.; Motley, J. R.; Tan, X.; Pholsena, K.; Árnadóttir, L.; Castle, J. R.; Jacobs, P. G.; Cargill, R. S.; et al. Fabrication of a Flexible Amperometric Glucose Sensor Using Additive Processes. *ECS J. Solid State Sci. Technol.* **2015**, *4* (4), P3069–P3074.

(2) Yuan, Y.; Giri, G.; Ayzner, A. L.; Zoombelt, A. P.; Mannsfeld, S. C. B.; Chen, J.; Nordlund, D.; Toney, M. F.; Huang, J.; Bao, Z. Ultra-High Mobility Transparent Organic Thin Film Transistors Grown by an off-Centre Spin-Coating Method. *Nat. Commun.* **2014**, *5*, 1–9.

(3) Meng, D.; Sun, D.; Zhong, C.; Liu, T.; Fan, B.; Huo, L.; Li, Y.; Jiang, W.; Choi, H.; Kim, T.; et al. High-Performance Solution-Processed Non-Fullerene Organic Solar Cells Based on Selenophene-Containing Perylene Bisimide Acceptor http://pubs.acs.org/doi/abs/10.1021/jacs.5b11149 (accessed Mar 15, 2018).

(4) Krebs, F. C. Polymer Solar Cell Modules Prepared Using Roll-to-Roll Methods: Knife-over-Edge Coating, Slot-Die Coating and Screen Printing. *Sol. Energy Mater. Sol. Cells* **2009**, *93* (4), 465–475.

(5) C. Krebs, F.; Tromholt, T.; Jørgensen, M. Upscaling of Polymer Solar Cell Fabrication Using Full Roll-to-Roll Processing. *Nanoscale* **2010**, *2* (6), 873–886.

(6) Krebs, F. C. All Solution Roll-to-Roll Processed Polymer Solar Cells Free from Indium-Tin-Oxide and Vacuum Coating Steps. *Org. Electron.* **2009**, *10* (5), 761–768.

(7) Søndergaard, R. R.; Hösel, M.; Krebs, F. C. Roll-to-Roll Fabrication of Large Area Functional Organic Materials. *J. Polym. Sci. Part B Polym. Phys.* **2013**, *51* (1), 16–34.

(8) van Oosten, C. L.; Bastiaansen, C. W. M.; Broer, D. J. Printed Artificial Cilia from Liquid-Crystal Network Actuators Modularly Driven by Light. *Nat. Mater.* **2009**, *8* (8), 677–682.

(9) Ishii, H.; Sugiyama, K.; Ito, E.; Seki, K. Energy Level Alignment and Interfacial Electronic Structures at Organic/Metal and Organic/Organic Interfaces. *Adv. Mater.* **1999**, *11* (8), 605–625.

(10) Braun, S.; Salaneck, W. R.; Fahlman, M. Energy-Level Alignment at Organic/Metal and Organic/Organic Interfaces. *Adv. Mater.* **2009**, *21*, 1450–1472.

(11) Campbell, I. H.; Ruben, S.; Zawodzinski, T. A.; Kress, J. D.; Martin, R. L.; Smith, D. L.; Barashkov, N. N.; Ferraris, J. P. Controlling Schottky Energy Barriers in Organic Electronic Devices Using Self-Assembled Monolayers. *Phys. Rev. B* **1996**, *54* (20), 14321–14324.

(12) Campbell, I. H.; Kress, J. D.; Martin, R. L.; Smith, D. L.; Barashkov, N. N.; Ferraris, J. P. Controlling Charge Injection in Organic Electronic Devices Using Self-Assembled Monolayers. *Appl. Surf. Sci.* **1997**, *71*, 3528–3530.

(13) Hong, J. P.; Park, A. Y.; Lee, S.; Kang, J.; Shin, N.; Yoon, D. Y. Tuning of Ag Work Functions by Self-Assembled Monolayers of Aromatic Thiols for an Efficient Hole Injection for Solution Processed Triisopropylsilylethynyl Pentacene Organic Thin Film Transistors. *Appl. Phys. Lett.* **2008**, *92*, 143311.

(14) Kitamura, M.; Kuzumoto, Y.; Aomori, S.; Kamura, M.; Na, J. H.; Arakawa, Y. Threshold Voltage Control of Bottom-Contact n-Channel Organic Thin-Film Transistors Using Modified Drain-Source Electrodes. *Appl. Phys. Lett.* **2009**, *94*, 083310.

(15) Halik, M.; Hirsch, A. The Potential of Molecular Self-Assembled Monolayers in Organic Electronic Devices. *Adv. Mater.* **2011**, *23*, 2689–2695.

(16) Schreiber, F. Self-Assembled Monolayers: From “simple” Model Systems to Biofunctionalized Interfaces. *J. Phys. Condens. Matter* **2004**, *16*, R881–R900.

(17) Irimia-Vladu, M. “Green” Electronics: Biodegradable and Biocompatible Materials and Devices for Sustainable Future. *Chem. Soc. Rev.* **2014**, *43*, 588–610.

(18) Russew, M. M.; Hecht, S. Photoswitches: From Molecules to Materials. *Adv. Mater.* **2010**, *22*, 3348–3360.

(19) Browne, W. R.; Kudernac, T.; Katsonis, N.; Areephong, J.; Hjelm, J.; Feringa, B. L. Electro- and Photochemical Switching of Dithienylethene Self-Assembled Monolayers on Gold Electrodes. *J. Phys. Chem. C* **2008**, *112*, 1183–1190.

(20) Browne, W. R.; Feringa, B. L. Light Switching on Molecules on Surfaces. *Annu. Rev. Phys. Chem.* **2009**, *60*, 407–428.

(21) Caldwell, W. B.; Campbell, D. J.; Chen, K.; Herr, B. R.; Mirkin, C. A.; Malik, A.; Durbin, M. K.; Dutta, P.; Huang, K. G. A Highly Ordered Self-Assembled Monolayer Film of an Azobenzenealkanethiol on Au(111): Electrochemical Properties and Structural Characterization by Synchrotron in-Plane x-Ray Diffraction, Atomic Force Microscopy, and Surface-Enhanced Raman Spectroscopy. *J. Am. Chem. Soc.* **1995**, *117* (22), 6071–6082.

(22) Suda, M.; Kameyama, N.; Ikegami, A.; Einaga, Y. Reversible Phototuning of the Large Anisotropic Magnetization at the Interface between a Self-Assembled Photochromic Monolayer and Gold. *J. Am. Chem. Soc.* **2009**, *131*, 865–870.

(23) Ah Qune, L. F. N.; Akiyama, H.; Nagahiro, T.; Tamada, K.; Wee, A. T. S. Reversible Work Function Changes Induced by Photoisomerization of Asymmetric Azobenzene Dithiol Self-Assembled Monolayers on Gold. *Appl. Phys. Lett.* **2008**, *93*, 083109.

(24) Nagahiro, T.; Akiyama, H.; Hara, M.; Tamada, K. Photoisomerization of Azobenzene Containing Self-Assembled Monolayers Investigated by Kelvin Probe Work Function Measurements. *J. Electron Spectrosc. Relat. Phenomenom* **2009**, *172*, 128–133.

(25) Crivillers, N.; Orgiu, E.; Reinders, F.; Mayor, M.; Samori, P. Optical Modulation of the Charge Injection in an Organic Field-Effect Transistor Based on Photochromic Self-Assembled-Monolayer-Functionalized Electrodes. *Adv. Mater.* **2011**, *23*, 1447–1452.

(26) Bartucci, M. A.; Florian, J.; Ciszek, J. W. Spectroscopic Evidence of Work Function Alterations Due to Photoswitchable Monolayer on Gold Surfaces. *J. Phys. Chem. C* **2013**, *117*, 19471–19476.

(27) Comstock, M. J.; Levy, N.; Kirakosian, A.; Cho, J.; Lauterwasser, F.; Harvey, J. H.; Strubbe, D. A.; Frechet, J. M. J.; Trauner, D.; Louis, S. G.; et al. Reversible

Photomechanical Switching of Individual Engineered Molecules at a Metallic Surface. *Phys. Rev. Lett.* **2007**, *99*, 038301.

(28) Hopwood, J. P.; Ciszek, J. W. Solid State and Surface Effects in Thin-Film Molecular Switches. *Photochem. Photobiol. Sci.* **2017**, *16* (7), 1095–1102.

(29) Forrest, S. R. The Path to Ubiquitous and Low-Cost Organic Electronic Appliances on Plastic. *Nature* **2004**, *428* (6986), 911–918.

(30) Facchetti, A. Semiconductors for Organic Transistors. *Mater. Today* **2007**, *10* (3), 28–37.

(31) Murphy, A. R.; Fréchet, J. M. J. Organic Semiconducting Oligomers for Use in Thin Film Transistors. *Chem. Rev.* **2007**, *107* (4), 1066–1096.

(32) Anthony, J. E. Functionalized Acenes and Heteroacenes for Organic Electronics. *Chem. Rev.* **2006**, *106* (12), 5028–5048.

(33) Anthony John E. The Larger Acenes: Versatile Organic Semiconductors. *Angew. Chem. Int. Ed.* **2007**, *47* (3), 452–483.

(34) Dimitrakopoulos C.D.; Malenfant P.R.L. Organic Thin Film Transistors for Large Area Electronics. *Adv. Mater.* **2002**, *14* (2), 99–117.

(35) Kim, Y.; Jeon, D. Real Time Monitoring of Ordering in Pentacene Films during Growth by Using In-Situ Infrared Spectroscopy. *Curr. Appl. Phys.* **2017**, *17*, 972–975.

(36) Watkins, N. J.; Yan, L.; Gao, Y. Electronic Structure Symmertry of Interfaces between Pentacene and Metals. *Appl. Phys. Lett.* **2002**, *80*, 4384–4389.

(37) Gundlach, D. J.; Zhou, L.; Nichols, J. A.; Jackson, T. N.; Necliudov, P. V.; Shur, M. S. An Experimental Study of Contact Effects in Organic Thin Film Transistors. *J. Appl. Phys.* **2006**, *100*, 024509.

(38) Park, S. K.; Jackson, T. N.; Anthony, J. E.; Mourey, D. A. High Mobility Solution Processed 6,13-Bis(Triisopropyl-Silylethynyl) Pentacene Organic Thin Film Transistors. *Appl. Phys. Lett.* **2007**, *91* (6), 063514.

(39) Giri, G.; Verploegen, E.; Mannsfeld, S. C. B.; Atahan-Evrenk, S.; Kim, D. H.; Lee, S. Y.; Becerril, H. A.; Aspuru-Guzik, A.; Toney, M. F.; Bao, Z. Tuning Charge Transport in Solution-Sheared Organic Semiconductors Using Lattice Strain. *Nature* **2011**, *480* (7378), 504–508.

(40) Seol, Y. G.; Lee, N.-E.; Park, S. H.; Bae, J. Y. Improvement of Mechanical and Electrical Stabilities of Flexible Organic Thin Film Transistor by Using Adhesive Organic Interlayer. *Org. Electron.* **2008**, *9* (3), 413–417.

(41) Tarlov, M. J. Silver Metalization of Octadecanethiol Monolayers Self-Assembled on Gold. *Langmuir* **1992**, *8* (1), 80–89.

(42) Herdt, G. C.; Jung, D. R.; Czanderna, A. W. Weak Interactions between Deposited Metal Overlayers and Organic Functional Groups of Self-Assembled Monolayers. *Prog. Surf. Sci.* **1995**, *50* (1), 103–129.

(43) Ohgi, T.; Sheng, H.-Y.; Nejoh, H. Au Particle Deposition Ont Self-Assembled Monolayers of Thiol and Dithiol Molecules. *Appl. Surf. Sci.* **1998**, *130*, 919–924.

(44) Piranej, S.; Turner, D. A.; Dalke, S. M.; Park, H.; Qualizza, B. A.; Vicente, J.; Chen, J.; Ciszek, J. W. Tunable Interfaces on Tetracene and Pentacene Thin-Films via Monolayers. *CrystEngComm* **2016**, *18* (32), 6062–6068.

(45) Orgiu, E.; Samori, P. Organic Electronics Marries Photochromism: Generation of Multifunctional Interfaces, Materials, and Devices. *Adv. Mater.* **2014**, *26*, 1827–1845.

(46) Ratner, M. Molecular Electronics: Pushing Electrons Around. *Nature* **2000**, *404*, 137–138.

(47) Ulman, A. Formation and Structure of Self-Assembled Monolayers. *Chem. Rev.* **1996**, *96*, 1533–1554.

(48) Vicario, J.; Katsonis, N.; Ramon, S.; Bastiaansen, C. W. M.; Broer, D. J.; Feringa, B. L. Nanomotor Rotates Microscale Objects. *Nature* **2008**, *440*, 163.

(49) Shirai, Y.; Minami, K.; Nakanishi, W.; Yonamine, Y.; Joachim, C.; Ariga, K. Driving Nanocars and Nanomachine at Interfaces: From Concept of Nanoarchitectonics to Actual Use in World Wide Race and Hand Operation. *Jpn. J. Appl. Phys.* **2016**, *55*, 1102A2.

(50) Durr, H. 4n+2 Systems Based on 1,5-Electrocyclization. In *Photochromism: Molecules and Systems*; Studies in Organic Chemistry; Elsevier Science Publishers B. V.: Amsterdam, The Netherlands, 1990; pp 210–269.

(51) Katsonis, N.; Kudernac, T.; Walko, M.; van der Molen, S. J.; van Wees, B. J.; Feringa, B. L. Reversible Conductance Switching of Single Diarylethenes on a Gold Surface. *Adv. Mater.* **2006**, *18*, 1397–1400.

(52) Kumar, A. S.; Ye, T.; Takami, T.; Yu, B.-C.; Flatt, A. K.; Tour, J. M.; Weiss, P. S. Reversible Photo-Switching of Single Azobenzene Molecules in Controlled Nanoscale Enviroments. *Nano Lett.* **2008**, *8*, 1644–1648.

(53) Durr, H. Perspectives in Photochromism: A Novel System Based on the 1,5-Electrocyclization of Heteroanalogous Pentadienyl Anions. *Angew. Chem. Int. Ed. Engl.* **1989**, *28*, 413–431.

(54) Napper, A. M.; Lui, H.; Waldeck, D. H. The Nature of Electronic Coupling between Ferrocene and Gold through Alkanethiolate Monolayers on Electrodes: The Importance of Chain Composition, Interchain Coupling, and Quantum Interference. *J. Phys. Chem. B* **2001**, *105*, 7699–7707.

(55) Wen, J.; Li, W.; Chen, S.; Ma, J. Simulations of Molecular Self-Assembled Monolayers on Surfaces: Packing Structures, Formation Processes and Function Tuned by Intermolecular and Interfacial Interactions. *Phys. Chem. Chem. Phys.* **2016**, *18*, 22757.

(56) Pourghaz, Y.; Dongare, P.; Thompson, D. W.; Zhao, Y. Click Functionalized Poly(p-Phenylene Ethynylene)s as Highly Selective and Sensitive Fluorescence Turn-on Chemosensors for Zn2+and Cd 2+ Ions. *Chem. Commun.* **2011**, *47*, 11014–11016.

(57) Evans, S. D.; Johnson, S. R.; Ringsdorf, H.; Williams, L. M.; Wolf, H. Photoswitching of Azobenzene Derivatives Formed on Planar and Colloidal Gold Surfaces. *Langmuir* **1998**, *14*, 6436–6440.

(58) Gahl, C.; Schmidt, R.; Brete, D.; McNellis, E. R.; Freyer, W.; Carley, R.; Reuter, K.; Weinelt, M. Structure and Excitonic Coupling in Self-Assembled Monolayers of Azobenzene-Functionalized Alkanethiols. *J. Am. Chem. Soc.* **2010**, *132*, 1831–1838.

(59) Zhou, X.-L.; Zhu, X.-Y.; White, J. M. Photochemistry at Adsorbate/Metal Interfaces. *Surf. Sci. Rep.* **1991**, *13*, 73–220.

(60) Bartucci, M. A.; Wierzbicki, P. M.; Gwengo, C.; Shajan, S.; Hussain, S. H.; Ciszek, J. W. Synthesis of Dihydroindolizines for Potential Photoinduced Work Function Alteration. *Tetrahedron Lett.* **2010**, *51*, 6839–6842.

(61) Wierzbicki, P. M. *Thesis*; Loyola University Chicago: Chicago, IL, 2011.

(62) Bartucci, M. A.; Ciszek, J. W. Substitent Parameters Impacting Isomer Composition and Optical Properties of Dihydroindolizine Molecular Switches. *J. Org. Chem.* **2014**, *79*, 5586–5594.

(63) Griffiths, P. R.; de Haseth, J. A. *Fourier Transform Infrared Spectrometry*; John Wiley & Sons, Inc.: Hoboken, NJ, 2007.

(64) Ree, M.; Chu, C.-W.; Goldberg, M. J. Influences of Chain Rigidity, in-Plane Orientation, and Thickness on Residual Stress of Polymer Films. *J. Appl. Phys.* **1994**, *75*, 1410–1419.

(65) Feringa, B. L.; Browne, W. R. *Molecular Switches*, Second Edition.; WILEY-VCH: Weinheim, Germany, 2011.

(66) Chance, R. R.; Prock, A.; Silbey, R. Comments on the Classical Theory of Energy Transfer. *J. Chem. Phys.* **1975**, *62*, 2245–2253.

(67) Yun, C. S.; Javier, A.; Jennings, T.; Fisher, M.; Hira, S.; Peterson, S.; Hopkins, B.; Reich, N. O.; Strouse, G. F. Nanometal Surface Energy Transfer in Optical Rulers, Breaking the FRET Barrier. *J. Am. Chem. Soc.* **2005**, *127*, 3115–3119.

(68) Rasnik, I.; McKinney, S. A.; Ha, T. Surfaces and Orientations: Much to FRET About? *Acc. Chem. Res.* **2005**, *28*, 542–548.

(69) Saini, S.; Singh, H.; Bagchi, B. Fluorescence Resonance Energy Transfer (FRET) in Chemistry and Biology: Non-Forster Distance Dependence of the FRET Rate. *J. Chem. Sci.* **2006**, *118*, 23–25.

(70) Moth-Poulsen, K.; Patrone, L.; Stuhr-Hansen, N.; Christensen, J. B.; Bourgoin, J.-P.; Bjornholm, T. Probing the Effects of Conjugation Path on the Electronic Transmission through Single Molecules Using Scanning Tunneling Microscopy. *Nano Lett.* **2005**, *5*, 783–785.

(71) Bilewicz, R.; Majda, M. Monomolecular Langmuir-Blodgett Films at Electrodes. Formation of Passivating Monolayers and Incorporation of Electroactive Reagents. *Langmuir* **1991**, *7*, 2794–2802.

(72) Templeton, A. C.; Wuelfing, W. P.; Murray, R. W. Monolayer-Protected Cluster Molecules. *Acc. Chem. Res.* **2000**, *33*, 27–36.

(73) Wold, D. J.; Haag, R.; Rampi, M. A.; Frisbie, C. D. Distance Dependence of Electron Tunneling through Self-Assembled Monolayers Measured by Conducting Probe Atomic Force Microscopy: Unsaturated versus Saturated Molecular Junctions. *J. Phys. Chem. B* **2002**, *106*, 2813–2816.

(74) Akkerman, H. B.; Blom, P. W. M.; de Leeuw, D. M.; de Boer, B. Towards Molecular Electronics with Large-Area Molecular Junctions. *Nature* **2006**, *441*, 69–72.

(75) Ma, H.; Yip, H.-L.; Huang, F.; Jen, A. K.-Y. Interface Engineering for Organic Electronics. *Adv. Funct. Mater.* **2010**, *20*, 1371–1388.

(76) Zhou, Y.; Fuentes-Hernandez, C.; Shim, J.; Meyer, J.; Giordano, A. J.; Li, H.; Winget, P.; Papadopoulos, T.; Cheun, H.; Kim, J.; et al. A Universal Method to Produce Low–Work Function Electrodes for Organic Electronics. *Science* **2012**, *336*, 327–332.

(77) Kobayashi, S.; Nishikawa, T.; Takenobu, T.; Mori, S.; Shimoda, T.; Mitani, T.; Shimotani, H.; Yoshimoto, N.; Ogawa, S.; Iwasa, Y. Control of Carrier Density by Self-Assembled Monolayers in Organic Field-Effect Transistors. *Nat. Mater.* **2004**, *3*, 317–322.

(78) Yoneya, N.; Noda, M.; Hirai, N.; Nomoto, K.; Wada, M.; Kasahara, J. Reduction of Contact Resistance in Pentacene Thin-Film Transistors by Direct Carrier Injection into a-Few-Molecular-Layer Channel. *Appl. Phys. Lett.* **2004**, *85*, 4663–4665.

(79) de Boer, B.; Hadipour, A.; Mandoc, M. M.; van Woudenbergh, T.; Blom, P. W. M. Tuning of Metal Work Functions with Self-Assembled Monolayers. *Adv. Mater.* **2005**, *17* (5), 621–625.

(80) Youn, J.; Dholakia, G. R.; Huang, H.; Henneck, J. W.; Facchetti, A.; Marks, T. J. Influence of Thiol Self-Assembled Monolayer Processing on Bottom-Contact Thin-Film Transistors Based on n-Type Organic Semiconductors. *Adv. Funct. Mater.* **2012**, *22* (9), 1856–1869.

(81) Smits, E. C. P.; Mathijssen, S. G. J.; van Hal, P. A.; Setayesh, S.; Geuns, T. C. T.; Mutsaers, K. A. H. A.; Cantatore, E.; Wondergem, H. J.; Werzer, O.; Resel, R.; et al. Bottom-up Organic Integrated Circuits. *Nature* **2008**, *455*, 956–959.

(82) Cernetic, N.; Acton, O.; Weidner, T.; Hutchings, D. O.; Baio, J. E.; Ma, H.; Jen, A. K.-Y. Bottom-Contact Small-Molecule n-Type Organic Field Effect Transistors Achieved via Simultaneuous Modification of Electrode and Dielectic Surfaces. *Org. Electron.* **2012**, *13* (12), 3226–3233.

(83) Burrows, P. E.; Bulovic, V.; Forrest, S. R.; Sapochak, L. S.; McCarty, D. M.; Thompson, D. W. Reliability and Degradation of Organic Light Emitting Devices. *Appl. Phys. Lett.* **1994**, *65* (23), 2922–2924.

(84) Hung, L. S.; Chen, C. H. Recent Progress of Molecular Organic Electroluminescent Materials and Devices. *Mater. Sci. Eng. R* **2002**, *39*, 143–222.

(85) Cho, J. H.; Lim, J. A.; Han, J. T.; Jan, H. W.; Lee, J.-L.; Cho, K. Control of the Electrical and Adhesion Properties of Metal/Organic Interfaces with Self-Assembled Monolayers. *Appl. Phys. Lett.* **2005**, *86*, 171906.

(86) Calhoun, M. F.; Sanchez, J.; Olaya, D.; Gershenson, M. E.; Podzorov, V. Electronic Functionalization of the Surface of Organic Semiconductors with Self-Assembled Monolayers. *Nat. Mater.* **2008**, *7*, 84–89.

(87) Piranej, S.; Turner, D. A.; Dalke, S. M.; Park, H.; Qualizza, B. A.; Vicente, J.; Chen, J.; Ciszek, J. W. Tunable Interfaces on Tetracene and Pentacene Thin-Films via Monolayers. *Cryst. Eng. Commun.* **2016**, *18*, 6062.

(88) Qualizza, B. A.; Prasad, S.; Chiarelli, M. P.; Ciszek, J. W. Functionalization of Organic Semiconductor Crystals via the Diels-Alder Reaction. *Chem. Commun.* **2013**, *49*, 4495.

(89) Lee, B.; Chen, Y.; Duerr, F.; Mastrogiovanni, D.; Garfunkel, E.; Andrei, E. Y.; Podzorov, V. Modification of Electronic Properties of Graphene with Self-Assembled Monolayers. *Nano Lett.* **2010**, *10*, 2427–2432.

(90) Herdt, G. C.; Jung, D. R.; Czanderna, A. W. Weak Interactions between Deposited Metal Overlayers and Organic Functional Groups of Self-Assembled Monolayers. *Prog. Surf. Sci.* **1995**, *50*, 103–129.

(91) Su, J.; Mrksich, M. Using Mass Spectrometry to Characterize Self-Assembled Monolayers Presenting Peptides, Proteins, and Carbohydrates. *Angew. Chem. Int. Ed.* **2002**, *41*, 4715–4718.

(92) Stutzmann, M.; Garrido, J. A.; Eickhoff, M.; Brandt, M. S. Direct Biofunctionalization of Semiconductors: A Survey. *Physic Status Solidi A* **2006**, *203*, 3424–3437.

(93) Lee, H.; Dellatore, S. M.; Miller, W. M.; Messersmith, P. B. Mussel-Inspired Surface Chemistry for Multifunctional Coatings. *Science* **2007**, *318* (5849), 426–430.

(94) Dupin, J.-C.; Gonbeau, D.; Vinatier, P.; Levasseur, A. Systematic XPS Studies of Metal Oxides, Hydroxides and Peroxides. *Phys. Chem. Chem. Phys.* **2000**, *2* (6), 1319–1324.

(95) Smith, M. B.; March, J. *March's Advanced Organic Chemistry: Reactions, Mechanisms, and Structure*, 5th ed.; John Wiley & Sons, Inc.: New York, NY, 2001.

(96) Coleman, L. E.; Bork, J. F.; Dunn, H. Reaction of Primary Aliphatic Amines with Maleic Anhydride. *J. Org. Chem.* **1959**, *24*, 135–136.

(97) Emsley, J. Very Strong Hydrogen Bonding. *Chem. Soc. Rev.* **1980**, *9*, 91–124.

(98) Zeergers-Huyskens, T.; Sobczyk, L. Critical Behavoir of Strong Hydrogen Bonds and the Isotopic Effects. *J. Mol. Liq.* **1990**, *46*, 263–284.

(99) Kawaguchi, S.; Kitano, T.; Ito, K. Infrared and Ultraviolet Spectroscopic Studies on Intramolecular Hydrogen Bonding in an Alternating Copolymer of Isobutylene and Maleic Acid. *Macromolecules* **1991**, *24*, 6030–6036.

(100) Eberson, L. Studies on Succinic Acids IV.* Evidence for the Existence of Intramolecular Hydrogen Bonding in Certain Highly Alkylated Succinic Acids by Infra-Red Spectra. *Acta Chem. Scand.* **1959**, *13*, 224–235.

(101) Ilczyszyn, M.; Godzisz, D.; Ilczyszyn, M. M. Sarcosine-Maleic Acid (1:1) Crystal: Structure, 13C NMR and Vibrational Properites, Protonation Character. *Spectrochim. Acta Part A* **2003**, *59*, 1815–1828.

(102) Cardwell, H. M. E.; Dunitz, J. D.; Orgel, L. E. The Structure of the Hydrogen Maleate Anion: A Symmetric Hydrogen Bond? *J. Chem. Soc.* **1953**, *0*, 3740–3742.

(103) Li, D.; Borkent, E.-J.; Nortrup, R.; Moon, H.; Katz, H.; Bao, Z. Humidity Effect on Electrical Performance of Organic Thin-Film Transistors. *Appl. Phys. Lett.* **2005**, *86* (4), 042105.

(104) Che, Y.; Yang, X.; Loser, S.; Zang, L. Expedient Vapor Probing of Organic Amines Using Fluorescent Nanofibers Fabricated from an N-Type Organic Semiconductor. *Nano Lett.* **2008**, *8* (8), 2219–2223.

(105) Brandon, D.; Kaplan, W. D. *Microstructural Characterization of Materials*, Second Edition.; John Wiley & Sons, Inc.: England, 2008.

(106) Stepanow, S.; Strunskus, T.; Lingenfelder, M.; Dmitriev, A.; Spillmann, H.; Lin, N.; Barth, J. V.; Wöll, C.; Kern, K. Deprotonation-Driven Phase Transformations in Terephthalic Acid Self-Assembly on Cu(100). *J. Phys. Chem. B* **2004**, *108* (50), 19392–19397.

(107) Jansen, R. J. J.; van Bekkum, H. XPS of Nitrogen-Containing Functional Groups on Activated Carbon. *Carbon* **1995**, *33* (8), 1021–1027.

(108) Stevens, J. S.; Byard, S. J.; Seaton, C. C.; Sadiq, G.; Davey, R. J.; Schroeder, S. L. M. Proton Transfer and Hydrogen Bonding in the Organic Solid State: A Combined XRD/XPS/SsNMR Study of 17 Organic Acid–Base Complexes. *Phys. Chem. Chem. Phys.* **2013**, *16* (3), 1150–1160.

(109) Jesdinszki, M.; Struller, C.; Rodler, N.; Blondin, D.; Cassio, V.; Kucukpinar, E.; Langowski, H.-C. Evaluation of Adhesion Strength Between Thin Aluminum Layer and Poly(Ethylene Terephthalate) Substrate by Peel Tests - A Practical Apporach for the Packaging Industry. *J. Adhes. Sci. Technol.* **2012**, *26*, 2357–2380.

(110) Fulmer, G. R.; Miller, A. J. M.; Sherden, N. H.; Gottlieb, H. E.; Nudelman, A.; Stoltz, B. M.; Bercaw, J. E.; Goldberg, K. I. NMR Chemical Shifts of Trace Impurities: Common Laboratory Solvents, Organics, and Gases in Deuterated Solvents Relevant to the Organometallic Chemist. *Organometallics* **2010**, *29* (9), 2176–2179.

VITA

Jonathan P. Hopwood was born in London, United Kingdom and was raised on the island of Bermuda. Before attending Loyola University Chicago for his graduate studies, he attended Wheaton College in Wheaton, Illinois where he received a B.S. in Chemistry in 2013. While at Loyola University Chicago, Hopwood received the Arthur J. Schmitt Fellowship for the 2017-2018 academic year, which is awarded to Ph.D. candidates that are in the concluding year of their dissertations. Currently, Hopwood hopes to continue advancing chemistry and science as he moves on from his graduate studies.